Black hole-neutron star binaries in general relativity: effects of neutron star spin

Keisuke Taniguchi,[1] Thomas W. Baumgarte,[2, *] Joshua A. Faber,[1, †] and Stuart L. Shapiro[1, ‡]

[1]*Department of Physics, University of Illinois at Urbana-Champaign, Urbana, Illinois 61801, USA*
[2]*Department of Physics and Astronomy, Bowdoin College, Brunswick, Maine 04011, USA*
(Dated: October 24, 2007)

We present new sequences of general relativistic, quasiequilibrium black hole-neutron star binaries. We solve for the gravitational field in the conformal thin-sandwich decomposition of Einstein's field equations, coupled to the equations of relativistic hydrostatic equilibrium for a perfect fluid. We account for the black hole by solving these equations in the background metric of a Schwarzschild black hole whose mass is much larger than that of the neutron star. The background metric is treated in Kerr-Schild as well as isotropic coordinates. For the neutron star, we assume a polytropic equation of state with adiabatic index $\Gamma = 2$, and solve for both irrotational and corotational configurations. By comparing the results of irrotational and synchronized configurations with the same background metric, we conclude that the effect of the rotation on the location of tidal break-up is only on the order of a few percent. The different choices in the background also lead to differences of order a few percent, which may be an indication of the level to which these configurations approximate quasiequilibrium.

I. INTRODUCTION

Black hole-neutron star (hereafter BHNS) binary systems are, together with other compact binaries, among the most promising sources of gravitational waves for detection by ground-based interferometers such as LIGO [1], GEO600 [2], TAMA300 [3], and VIRGO [4], or for the planned space-based mission LISA [5]. Since theoretical predictions for the waveforms from such compact binaries are needed both for the identification and interpretation of any astrophysical signals, significant effort has gone into the theoretical modeling of these binaries and their inspiral (see [6, 7] for recent reviews).

The orbital separation of a BHNS binary decreases as energy and angular momentum are dissipated by the emission of gravitational radiation, which also has the effect of circularizing the orbit, until the system eventually coalesces. This coalescence can take two qualitatively different forms. If the neutron star reaches the innermost stable circular orbit (hereafter ISCO) while still stable against tidal disruption, it will likely plunge and fall into the black hole promptly. Alternately, if the neutron star is tidally disrupted outside the ISCO, the final fate may be a black hole surrounded by a disk. This model is a candidate central engine for short-period gamma-ray bursts, since the high efficiency of accretion onto a black hole can help to explain the huge luminosities seen in these sources [8, 9, 10]. Additionally, we may obtain information about the equation of state (hereafter EOS) of matter at nuclear densities through the detection of a gravitational wave signal, because the characteristic frequency at the tidal disruption separation is in the most sensitive range of the ground-based detectors [11].

The difference in the final fate is determined primarily by the mass ratio of the black hole to the neutron star. When the black hole mass M_{BH} is much larger than the neutron star mass M_{NS}, the tidal force from the black hole is not so large compared with the neutron star self-gravity to disrupt the neutron star, even at the ISCO. Indeed, the ISCO occurs at a radius proportional to the black hole mass, whereas the Roche limit separation, which would mark the beginning of mass transfer, scales like $M_{BH}^{1/3}$ in the limit of an extremely large mass ratio [12]. Thus, the larger the black hole mass, the further outward the ISCO lies relative to the Roche limit separation. On the other hand, a stellar mass black hole will have a tidal field sufficiently large with respect to the neutron star self-gravity to deform and disrupt the companion outside the ISCO. The critical value of the mass ratio falls in the range $M_{BH}/M_{NS} \sim 4$ for reasonable neutron star models [13], but varies depending on assumptions about the neutron star EOS (see [14] for a thorough discussion).

Until now, much effort has been devoted to the computation of the BHNS binary systems. Most dynamical simulations so far have been carried out in a Newtonian framework [8, 15, 16, 17, 18, 19, 20], but see [14, 21] for approximate relativistic treatments. Quasiequilibrium models of BHNS binaries have been constructed adopting various different approximations. Several authors (including [22]) have modeled BHNS binaries as Newtonian ellipsoids around point masses, generalizing the classic Roche model for incompressible stars [23]. These ellipsoidal calculations have also been generalized to include relativistic effects [13, 24, 25, 26, 27]. Recently, these

*Fellow of the J. S. Guggenheim Memorial Foundation; Also at: Department of Physics, University of Illinois at Urbana-Champaign, Urbana, Illinois 61801, USA
†National Science Foundation (NSF) Astronomy and Astrophysics Postdoctoral Fellow
‡Also at: Department of Astronomy and NCSA, University of Illinois at Urbana-Champaign, Urbana, Illinois 61801, USA

models have been generalized to include higher order deformations than ellipsoid by expanding the background black hole metric to higher order than quadrupole [28]. Equilibrium models of Newtonian BHNS binaries also have been constructed by solving the exact fluid equations numerically and again treating the black hole as a point-mass [29]. With the possible exception of [30], Baumgarte *et al.* [31] (hereafter BSS) so far provide the only self-consistent relativistic treatment of BHNS binaries in quasiequilibrium.

In BSS, BHNS binaries are constructed by solving the constraint equations of general relativity, decomposed in the conformal thin-sandwich formalism, together with the Euler equation for the neutron star matter, which takes an algebraic form if the system can be taken to be stationary in a corotating frame. The equations are solved in the background of a Schwarzschild black hole, which accounts for the neutron star's companion.

In this paper we generalize the findings of BSS in two ways. As discussed above we allow of irrotational instead of corotational fluid flow, which is more realistic astrophysically [32, 33]. To do so we adopt the formalism for constructing irrotational stars as developed in [34]. We also generalize the results of BSS by expressing the black hole background in a different coordinate system. In BSS, this background was expressed in Kerr-Schild coordinates, which we compare here with a black hole background expressed in isotropic coordinates. Since the two coordinate system represent different slicings of the Schwarzschild space-time, the resulting initial data are physically distinct solutions of the constraint equations. Finally, in this paper we adopt a numerical code that is based on the spectral method numerical libraries known as LORENE [35] (as opposed to the finite difference implementation of BSS). We maintain several of the other assumptions made by BSS, including extreme mass ratio $M_{\rm BH} \gg M_{\rm NS}$ and polytropic equations of state, and plan to relax these in the future.

The spectral techniques used here have previously been employed to compute quasiequilibrium sequences of binary neutron stars [34, 36, 37, 38, 39, 40]. There are several advantages in using spectral methods. One is that it is easy to treat spherical coordinates, which are suitable for solving figures like stars, and to fit the coordinates to trace the stellar surface. This fitting technique plays an important role in solving irrotational configurations. Another advantage is that it is possible to achieve more rapid convergence compared to finite difference methods, until configurations reach a separation very close to tidal break-up and the appearance of discontinuities in physical quantities (For more details on the spectral methods techniques we use, we refer the readers to [34, 41, 42].) In our code, the set of equations we solve for the gravitational field is essentially equivalent to that of BSS, while the hydrostatic equations are the same as those found in [34].

The paper is organized as follows. In Section II, we briefly summarize the formulation and explain the so-lution procedure. The tests of the numerical code are shown in Section III, and the results are presented in Section IV. In Section V we discuss the effects of the choice of the black hole background metric, and we summarize in Section VI.

Throughout the present paper, we adopt geometrical units, $G = c = 1$, where G denotes the gravitational constant and c the speed of light, respectively. Latin and Greek indices denote purely spatial and space-time components, respectively.

II. FORMULATION

In this Section we briefly discuss the basic equations, as well as their numerical implementation. For a more detailed discussion, we refer the reader to Section III of BSS for the gravitational fields (but point out some minor differences below) and to Section II of [34] for the hydrostatics. For corotating sequences using the Kerr-Schild metric, our notation will appear to be slightly different than that found in BSS, but the two sets of equations are completely equivalent, merely expressed in a different set of variables.

A. Gravitational field equations

The line element in 3+1 form is written as

$$
\begin{aligned}
ds^2 &= g_{\mu\nu}dx^\mu dx^\nu \\
&= -\alpha^2 dt^2 + \gamma_{ij}(dx^i + \beta^i dt)(dx^j + \beta^j dt), \quad (1)
\end{aligned}
$$

where α is the lapse function, β^i the shift vector, γ_{ij} the spatial metric, and $g_{\mu\nu}$ the space-time metric. The Einstein equations then split into two constraint equations – the Hamiltonian and the momentum constraint – and two evolution equations – one for the spatial metric γ_{ij} and one for the extrinsic curvature

$$
K_{ij} = -\frac{1}{2\alpha}\left(\partial_t \gamma_{ij} + D_i \beta_j + D_j \beta_i\right), \quad (2)
$$

where D_i denotes the covariant derivative associated with γ_{ij}. Using the conformal decomposition

$$
\gamma_{ij} = \psi^4 \tilde{\gamma}_{ij}, \quad (3)
$$

where ψ is the conformal factor and $\tilde{\gamma}_{ij}$ the background metric, the Hamiltonian constraint coupled with the trace part of the evolution equation of K^{ij} becomes

$$
\tilde{D}^2\sigma = 4\pi\psi^4 S + \frac{3}{4}\psi^{-8}\tilde{A}_{ij}\tilde{A}^{ij} + \frac{1}{4}\tilde{R} + \frac{1}{2}\psi^4 K^2
$$
$$
+\frac{\psi^4}{\alpha}\beta^i \tilde{D}_i K - \frac{1}{2}\tilde{\gamma}^{ij}\left[(\tilde{D}_i\nu)(\tilde{D}_j\nu) + (\tilde{D}_i\sigma)(\tilde{D}_j\sigma)\right], (4)
$$

where we have defined

$$
\sigma \equiv \ln(\alpha\psi^2); \quad (5)
$$

this quantity was denoted "β" in [34]. $\tilde{D}_i$, $\tilde{D}^2 = \tilde{\gamma}^{ij}\tilde{D}_i\tilde{D}_j$, $\tilde{R}_{ij}$, and $\tilde{R}$ are, respectively, the covariant derivative, covariant Laplace operator, Ricci tensor, and scalar curvature with respect to $\tilde{\gamma}_{ij}$. We have also decomposed the extrinsic curvature into its trace and traceless parts,

$$K^{ij} = \psi^{-10}\tilde{A}^{ij} + \frac{1}{3}\gamma^{ij}K. \tag{6}$$

In the derivation of (4) we have assumed $\partial_t K = 0$, which results in

$$\tilde{D}^2\nu = 4\pi\psi^4(\rho + S) + \psi^{-8}\tilde{A}_{ij}\tilde{A}^{ij} + \frac{1}{3}\psi^4 K^2$$
$$+ \frac{\psi^4}{\alpha}\beta^i\tilde{D}_i K - \tilde{\gamma}^{ij}(\tilde{D}_i\nu)(\tilde{D}_j\sigma) \tag{7}$$

for the quantity

$$\nu \equiv \ln\alpha. \tag{8}$$

Finally, we assume that $\partial_t\tilde{\gamma}_{ij} = 0$ for quasiequilibrium configuration, so that (2) yields

$$\tilde{A}^{ij} = \frac{\psi^6}{2\alpha}\left(\tilde{D}^i\beta^j + \tilde{D}^j\beta^i - \frac{2}{3}\tilde{\gamma}^{ij}\tilde{D}_k\beta^k\right). \tag{9}$$

Inserting this relation into the momentum constraint yields

$$\tilde{D}^2\beta^i + \frac{1}{3}\tilde{D}^i\tilde{D}_j\beta^j = 16\pi\alpha\psi^4 j^i - \tilde{R}^i_j\beta^j$$
$$+ \frac{4}{3}\alpha\tilde{D}^i K - \frac{2\alpha}{\psi^6}\tilde{A}^{ij}\tilde{D}_j(3\sigma - 4\nu). \tag{10}$$

The matter quantities on the right-hand side of equations (4), (7) and (10) are projections of the stress-energy tensor

$$T_{\mu\nu} = (\rho_0 + \rho_i + P)u_\mu u_\nu + Pg_{\mu\nu}, \tag{11}$$

where u_μ is the fluid 4-velocity, ρ_0 the baryon rest-mass density, ρ_i the internal energy density, and P the pressure. We then define

$$\rho \equiv n_\mu n_\nu T^{\mu\nu}, \tag{12}$$
$$j^i \equiv -\gamma^i_\mu n_\nu T^{\mu\nu}, \tag{13}$$
$$S_{ij} \equiv \gamma_{i\mu}\gamma_{j\nu}T^{\mu\nu}, \tag{14}$$
$$S \equiv \gamma^{ij}S_{ij}, \tag{15}$$

where $n_\mu = (-\alpha, 0, 0, 0)$ is the future-directed unit normal vector.

B. Background black hole metric

We account for the neutron star's black hole companion by choosing a background solution that represents a Schwarzschild metric. In BSS the Schwarzschild solution

was expressed in Kerr-Schild coordinates. In this paper we analyze the effect of this choice by comparing with the Schwarzschild background expressed in isotropic coordinates. Since the two coordinate system represent two distinct slicings of the Schwarzschild metric, we solve the constraint equations on different spatial slices, and therefore have no reason to expect that the resulting solutions to the constraint equations are physically identical.

TABLE I: Lapse function $\alpha_{\rm BH}$, shift vector $\beta^i_{\rm BH}$, conformal factor $\psi_{\rm BH}$, and the conformally related spatial metric $\tilde{\gamma}_{ij}$ for the Schwarzschild metric in Kerr-Schild (K-S) and isotropic (ISO) coordinates. $M_{\rm BH}$ is the black hole mass, $r_{\rm BH} = \sqrt{X^2 + Y^2 + Z^2}$ the distance from the black hole center, and we define $H_{\rm BH} \equiv M_{\rm BH}/r_{\rm BH}$ and $l_i = l^i \equiv X^i/r_{\rm BH}$. Note that $r_{\rm BH}$ in Kerr-Schild coordinates indicates a different displacement than one measured in isotropic ones.

	K-S	ISO
$\alpha_{\rm BH}$	$(1 + 2H_{\rm BH})^{-1/2}$	$\dfrac{1 - H_{\rm BH}/2}{1 + H_{\rm BH}/2}$
$\beta^i_{\rm BH}$	$2\alpha^2_{\rm BH}H_{\rm BH}l^i$	0
$\psi_{\rm BH}$	1	$1 + H_{\rm BH}/2$
$\tilde{\gamma}_{ij}$	$\eta_{ij} + 2H_{\rm BH}l_i l_j$	η_{ij}

In Table I we list the background metric quantities for both Kerr-Schild (KS) and isotropic (ISO) coordinates [43]. From these metric quantities a number of background quantities – for example $\tilde{R}^i_j$ and K – that enter equations (4), (7) and (10) are derived. For Kerr-Schild coordinates these quantities can be found in BSS; for isotropic coordinates they are either zero or trivial, since the background metric $\tilde{\gamma}_{ij}$ is flat and the shift vanishes.

To aid in the numerical solution we decompose the metric quantities into contributions from the neutron star and the black hole as follows. The total lapse function and conformal factor are decomposed into the product of a neutron star part and a black hole part (not a sum as in BSS), such that

$$\alpha = \alpha_{\rm NS}\alpha_{\rm BH}, \tag{16}$$
$$\psi = \psi_{\rm NS}\psi_{\rm BH}. \tag{17}$$

The neutron star part is calculated by solving Poisson-like equations while the black hole part is given by the background metric, shown in Table I. The product form is required in order to decompose ν and σ, defined by Eqs. (8) and (5), as a sum of the neutron star and black hole parts, such that

$$\nu = \nu_{\rm NS} + \nu_{\rm BH}, \tag{18}$$
$$\sigma = \sigma_{\rm NS} + \sigma_{\rm BH}, \tag{19}$$

where $\nu_{\rm NS} \equiv \ln\alpha_{\rm NS}$, $\nu_{\rm BH} \equiv \ln\alpha_{\rm BH}$, $\sigma_{\rm NS} \equiv \ln(\alpha_{\rm NS}\psi^2_{\rm NS})$, and $\sigma_{\rm BH} \equiv \ln(\alpha_{\rm BH}\psi^2_{\rm BH})$. The decomposition (16) and (17) are different from those employed by BSS, but formally equivalent.

For the shift vector, we decompose as

$$\beta^i = \beta^i_{\mathrm{NS}} + \beta^i_{\mathrm{BH}} + \beta^i_{\mathrm{rot}}, \tag{20}$$

where β^i_{NS} and β^i_{BH} are the neutron star and black hole contributions to the shift vectors seen by the inertial observer, and β^i_{rot} is the rotating shift vector defined as

$$\beta^i_{\mathrm{rot}} = \epsilon^{ijk}\Omega_j X_k = \Omega(-Y,\ X,\ 0), \tag{21}$$

where Ω_j is the orbital angular velocity vector. We define the Z-axis to be parallel to the rotation axis, so that $\Omega^i = (0,0,\Omega)$ in Cartesian coordinates.

As in BSS, we assume extreme mass ratios $M_{\mathrm{BH}} \gg M_{\mathrm{NS}}$, which simplifies the problem in several ways. In this limit, we may assume that the neutron star affects the space-time only in a region around the neutron star itself, so that we can restrict the computational domain to a neighborhood of the neutron star. This means that we do not need excise a black hole singularity from the numerical grid. We may also assume that the rotation axis coincides with the center of the black hole, which eliminates the need for an iteration to locate the axis of rotation (see Fig. 1).

For the isotropic background, the solution is symmetric both across the equatorial plane (i.e. the X–Y plane) and the X–Z plane. As discussed in BSS and [44], the presence of a non-vanishing trace of the extrinsic curvature eliminates the symmetry across the X–Z plane for a Kerr-Schild background, so that in the latter case we can assume a symmetry only across the equatorial plane.

Evidently, the numerical implementation of the isotropic background is much easier than that of the Kerr-Schild background. However, isotropic coordinates have the disadvantage that the lapse α_{BH} vanishes on the black hole horizon, which would cause problems in (9) when the black hole is included in the computational domain. The same property also causes problems in dynamical simulations, when these quasiequilibrium models are used as initial data (thus, in [14], Poisson-like equations are solved for ψ and $\alpha\psi$, as in BSS). Kerr-Schild coordinates have the advantage that the coordinates smoothly extend into the black hole interior, which eliminates both of these problems.

The above decompositions are then inserted into equations (4), (7) and (10), which are then solved for the neutron star contributions. We list the resulting equations in Appendix A.

C. Hydrostatic equations

For the cases considered here, the equations of relativistic hydrodynamics reduce to the the integrated Euler equation as well as the equation of continuity (which is satisfied identically for corotating stars). There are many sets of notation used to describe this formulation [45, 46, 47, 48, 49], but we follow that of [34], with one important exception: we denote the adiabatic index of
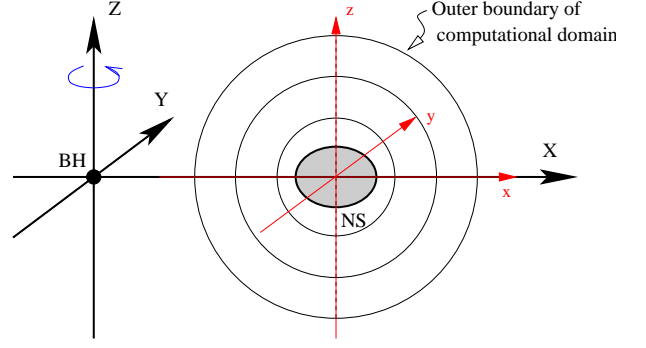

FIG. 1: Coordinate systems. The origin of the "global" coordinates (X, Y, Z) is located at the center of the black hole, and that of the "local" coordinates (x, y, z) at the point of maximum density within the neutron star. Here, we assume an extreme mass ratio $M_{\mathrm{BH}} \gg M_{\mathrm{NS}}$, so that the rotation axis of the orbit coincides with the center of the black hole. We define the Z-axis to point in the direction of the rotation axis. The relation between the global and local coordinates is given by $X = x + X_{\mathrm{NS}}$, $Y = y$, and $Z = z$, where X_{NS} denotes the orbital separation between the black hole and the neutron star.

our polytropic EOS by Γ and the Lorentz factor of the matter by γ, whereas their notation defines them the other way around.

1. Integrated Euler equation

The first integral of the Euler equation, common to both corotating and irrotational configurations, can be written as

$$h\alpha\frac{\gamma}{\gamma_0} = \mathrm{constant}, \tag{22}$$

where $h = (\rho_0 + \rho_i + P)/\rho_0$ is the fluid specific enthalpy. Here γ is the Lorentz factor between the fluid and the co-orbiting observer and γ_0 that between the co-orbiting observer and the inertial frame. Here we define the "inertial" frame as the frame corresponding to normal observers for whom the shift vector goes to zero at large r_{BH}. For the co-orbiting frame, normal observers satisfy $\beta^i \to (\Omega \times r_{\mathrm{BH}})^i$ at large r_{BH}. A detailed derivation can be found, for example, in [34]. The Lorentz factors can be written as

$$\gamma = \gamma_{\mathrm{n}}\gamma_0(1 - \gamma_{ij}U^i U_0^j), \tag{23}$$

$$\gamma_0 = (1 - \gamma_{ij}U_0^i U_0^j)^{-1/2}, \tag{24}$$

$$\gamma_{\mathrm{n}} = (1 - \gamma_{ij}U^i U^j)^{-1/2}, \tag{25}$$

where U_0^i is the orbital 3-velocity with respect to the inertial observer, given by $U_0^i = \beta^i/\alpha$, where the shift vector β^i is measured by a co-orbiting observer. The quantity γ_{n} denotes the Lorentz factor between the fluid and the inertial observer, and can also be expressed as

$\gamma_{\mathrm{n}} = \alpha u^t$ where u^t is the time component of the fluid 4-velocity u^μ. The quantity U^i is the fluid 3-velocity with respect to the inertial observer (see Eq. (27) of [34]); for corotating binary systems, the fluid 3-velocity seen by the co-orbiting observer vanishes, we obtain $U^i = U^i_0$. For irrotational binary systems, U^i can expressed in terms of a velocity potential Ψ as

$$U^i = \frac{1}{\gamma_{\mathrm{n}} h} D^i \Psi, \tag{26}$$

where D_i is the covariant derivative with respect to γ_{ij}. In this case, γ_{n} is written as

$$\gamma_{\mathrm{n}} = \left(1 + \frac{\gamma^{ij} D_i \Psi D_j \Psi}{h^2}\right)^{1/2}. \tag{27}$$

Taking the logarithm of Eq. (22), we obtain the final form of the integrated Euler equation,

$$H_{\mathrm{ent}} + \nu - \ln \gamma_0 + \ln \gamma = \text{constant}, \tag{28}$$

where $H_{\mathrm{ent}} \equiv \ln h$. For corotating binary systems we have $\gamma = 1$ and hence $\ln \gamma = 0$.

2. Equation of continuity

Having taken into account the helical symmetry, we rewrite the equation of continuity

$$\frac{n}{h} \nabla^\mu \nabla_\mu \Psi + (\nabla^\mu \Psi) \nabla_\mu \left(\frac{n}{h}\right) = 0, \tag{29}$$

where n is the fluid baryon number density and ∇_μ the covariant derivative associated with $g_{\mu\nu}$, in the 3+1 form

$$n D^i D_i \Psi + (D^i n)(D_i \Psi) = h \gamma_{\mathrm{n}} U^i_0 D_i n$$
$$+ n \left[(D^i \Psi) D_i \left(\ln \frac{h}{\alpha}\right) + h U^i_0 D_i \gamma_{\mathrm{n}}\right] + n h K \gamma_{\mathrm{n}}. \tag{30}$$

Introducing an auxiliary quantity which represents the logarithmic derivative of enthalpy with respect to baryon number density,

$$\zeta \equiv \frac{d \ln H_{\mathrm{ent}}}{d \ln n}, \tag{31}$$

we can rewrite Eq. (30) as

$$\zeta H_{\mathrm{ent}} \tilde{D}^2 \Psi + \tilde{\gamma}^{ij} \tilde{D}_j H_{\mathrm{ent}} \tilde{D}_i \Psi = \psi^4 h \gamma_{\mathrm{n}} U^i_0 \tilde{D}_i H_{\mathrm{ent}}$$
$$+ \zeta H_{\mathrm{ent}} \left[\tilde{\gamma}^{ij} \tilde{D}_j \Psi \tilde{D}_i (H_{\mathrm{ent}} - \sigma) + \psi^4 h U^i_0 \tilde{D}_i \gamma_{\mathrm{n}}\right.$$
$$\left. + \psi^4 h K \gamma_{\mathrm{n}}\right]. \tag{32}$$

We will show the final form of equations for the cases of the Kerr-Schild and isotropic coordinates in Appendices A 1 b and A 2 b.

D. Equation of state

We adopt a polytropic EOS for the neutron star of the form

$$P = \kappa \rho_0^\Gamma, \tag{33}$$

where Γ denotes the adiabatic index and κ is a constant. All results shown in this paper are for $\Gamma = 2$. Since dimensions enter the problem only through κ, it is convenient to rescale all dimensional quantities with respect to the length scale

$$R_{\mathrm{poly}} \equiv \kappa^{1/2(\Gamma-1)}. \tag{34}$$

For later comparison with the results of BSS, we also introduce the dimensionless quantity

$$q \equiv \frac{P}{\rho_0}, \tag{35}$$

in terms of which we can express the baryon rest-mass density and the pressure as

$$\rho_0 = R_{\mathrm{poly}}^{-2} q^{1/(\Gamma-1)}, \tag{36}$$
$$P = R_{\mathrm{poly}}^{-2} q^{\Gamma/(\Gamma-1)}. \tag{37}$$

E. Boundary condition

For any Poisson-like elliptic equation of the form

$$\underline{\Delta} \Phi = s, \tag{38}$$

where s is a source term with compact support, we can express the exterior solution as

$$\Phi(r, \theta, \varphi) = \sum_{l=0}^\infty \sum_{m=-l}^l s_{lm} Y_{lm}(\theta, \varphi) r^{-(l+1)}, \tag{39}$$

Here, s_{lm} are the multipole moments, defined as

$$s_{lm} \equiv \int_0^{R_{\mathrm{B}}} s r^l Y_{lm}^*(\theta, \varphi) d^3 x, \tag{40}$$

and where R_{B} is the extent of the non-zero domain of the source term. The source terms of the Poisson-like equations (A1) – (A3) or (A12) – (A14) are not compact in the situation we consider; however, since they fall off with a steep power-law dependence on the radius, ignoring the contribution from outside the computational domain introduces only minimal errors. In our code we match the numerical solution to (39) at the outer boundaries, which we refer to as a multipole boundary condition.

We truncate the expansion of the solution at a pre-determined value $l = l_{\mathrm{max}}$, here setting $l_{\mathrm{max}} = 4$ throughout. We set $s_{lm} = 0$ for all terms with $l > l_{\mathrm{max}}$.

Multipole boundary conditions, which allow us to achieve much greater accuracy, are convenient in spectral

applications, but less so in finite difference implementations. BSS, for example, used Robin boundary conditions which enforce that fields fall of with a certain power of $1/r$. In Sec. III A 2, we will compare the results of these two boundary conditions (and we also refer to [14] for a more detailed discussion of the boundary conditions).

F. Determination of the orbital angular velocity

To determine the orbital angular velocity, we require a force balance along the X-axis at the center of the neutron star,

$$\frac{\partial H_{\text{ent}}}{\partial X}\bigg|_{(X_{\text{NS}},0,0)} = 0, \tag{41}$$

where X_{NS} is the X-coordinate of the center of the neutron star relative to the black hole. Equation (41) means that the neutron star has its maximum enthalpy (and thus density) at the position $(X_{\text{NS}}, 0, 0)$, which corresponds to the origin of the local coordinate system (x, y, z) in which we solve the equations (see Fig. 1).

Inserting Eq. (28) into the condition (41), we obtain

$$\frac{\partial}{\partial X}\ln\gamma_0\bigg|_{(X_{\text{NS}},0,0)} = \frac{\partial}{\partial X}(\nu + \ln\gamma)\bigg|_{(X_{\text{NS}},0,0)}. \tag{42}$$

Equation (42) is solved algebraically for the orbital angular velocity Ω, which enters through the Lorentz factors and the shift decomposition (20) on both sides of the equation. We leave the dependence implicit on the right-hand side, but write out the dependence explicitly on the left-hand side (see Appendices A 1 c and A 2 c).

G. Global Integrals

It is reasonable to assume that during the binary inspiral both the neutron star's rest-mass and the black hole's irreducible mass are conserved. The rest mass is defined as

$$M_{\text{NS}} = \int \rho_0 u^t \sqrt{-g}\, d^3x, \tag{43}$$

$$= \int \rho_0 \alpha u^t \psi^6 \sqrt{\tilde{\gamma}}\, d^3x, \tag{44}$$

where g is the determinant of $g_{\mu\nu}$ and $\tilde{\gamma}$ that of $\tilde{\gamma}_{ij}$. The determinant $\tilde{\gamma}$ takes the form

$$\tilde{\gamma} = \begin{cases} 1 + 2H_{\text{BH}} & \text{for the K–S background,} \\ 1 & \text{for the flat background.} \end{cases} \tag{45}$$

In polytropic units (see Eq. (34)), we can normalize the baryon rest-mass in dimensionless form

$$\bar{M}_{\text{NS}} \equiv \frac{M_{\text{NS}}}{R_{\text{poly}}}. \tag{46}$$

Assuming extreme mass ratios allows us to neglect tidal effects of the neutron star on the black hole and to restrict the computational domain to a neighborhood of the neutron star. This means that we cannot evaluate the black hole's irreducible mass M_{irr}. Instead, we keep the background mass M_{BH} constant in this paper. The difference between M_{irr} and M_{BH} is of the order of the binary's binding energy (see footnote [35] in BSS), which is much smaller than either M_{irr} or M_{BH} in the limit of extreme mass ratios.

Other global integrals that we might be interested in are the ADM mass and the angular momentum, and especially their change along equilibrium sequences as a function of the binary separation. However, for the same reasons as explained in the previous paragraph, we cannot capture contributions of the binding energy to these quantities, meaning that we would find errors as large as the quantities that we are interested in. We therefore postpone evaluation of these integrals until we have relaxed the assumption of extreme mass ratios.
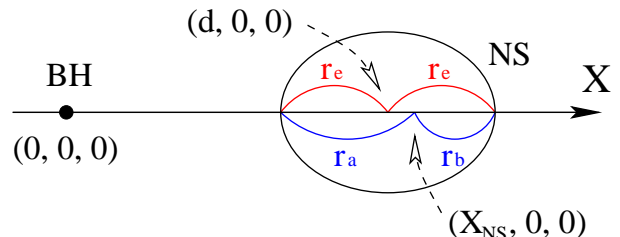

FIG. 2: Relation among the various neutron star "radii" r_e, r_a and r_b, as well as between the "orbital separations" X_{NS} and d. r_e is the half-diameter, which is defined as $r_e \equiv (r_a + r_b)/2$.

H. Solution procedure

We construct quasiequilibrium BHNS binaries in an iterative algorithm as follows. We start by preparing an initial guess, and then construct self-consistent solutions to the equations listed in Appendices A 1 and A 2 in an iteration that is similar to that of [34]. Since there are some differences in various steps of the process, however, it may be useful to describe the iteration in detail:

1. Preparation of initial data for the main iteration

   (a) Construct a spherical star in equilibrium.

   (b) Set the orbital separation between the center of the neutron star and the black hole to X_{NS}. Here, the center of the neutron star is located at the maximum of the enthalpy (and thus the density). As we assume an extreme mass ratio, the absolute coordinate of the center of the black hole is $(0, 0, 0)$, that of the neutron star $(X_{\text{NS}}, 0, 0)$; the rotation axis points in the

Z-direction, and goes through the origin of the absolute coordinate (see Fig. 1). At this stage, we set the black hole mass to a given constant $M_{\rm BH}$ and never change it during the main iteration that follows.

2. Main computation

(a) Introduce the black hole gravitational field as a fixed background.

(b) Set the initial guess of the orbital angular velocity to the Keplerian frequency.

(c) Solve the set of equations

    i. Gravitational field equations: Eqs. (A1) – (A3) for Kerr-Schild background; Eqs. (A12) – (A14) for isotropic background

    ii. Equation of continuity: Eq. (A10) for Kerr-Schild background; Eq. (A15) for isotropic background

(d) Determine the new enthalpy field from the integrated Euler equation, Eq. (28), and the new baryon rest-mass density from the neutron star EOS.

(e) Calculate the orbital angular velocity from Eq. (42) by solving it algebraically.

(f) Re-scale the radius of the neutron star and fit the outer boundary of the innermost domain to the surface of the neutron star.

(g) Change the orbital separation to have the same ratio of $X_{\rm NS}/r_e$ as the initially given value. Here r_e is the half-diameter of the neutron star on the *X*-axis (see Fig. 2).

(h) Change the central enthalpy to fix the baryon rest-mass of the neutron star at a given value $M_{\rm NS}$.

(i) Compare the new enthalpy field with that of old one, and check whether the relative difference is smaller than the threshold or not.

(j) If the condition (2i) is not satisfied, go back to (2c) and continue.

The lack of a symmetry across the $X-Z$ plane for a Kerr-Schild background introduces one more subtlety. The procedure we introduced above determines all the eigenvalues which appear in the present case, i.e., the orbital angular velocity, the radius of the neutron star, and the integration constant of the Euler equation. However, the above procedure does not include a method to fix the position of the neutron star in the local coordinate system (x, y, z), in which we solve the field equations. Thanks to the $X-Y$ plane symmetry (equatorial symmetry), the center of the neutron star is automatically located in the $X-Y$ plane. Additionally, the procedure for determination of the orbital angular velocity (2e) fixes the local

maximum of the neutron star rest-mass density along the *X*-axis at $X = X_{\rm NS}$ $(x = 0)$. Lacking an additional constraint, the neutron star center can fall at any position in the *Y*-direction, so long as the *X*-coordinate takes the proper value. To define our configurations unambiguously, we must require that the position we impose in the procedure (2e) is the *global* maximum of the neutron star rest-mass density. This requires the *Y*-derivative of the enthalpy to be zero as well as the *X*-derivative at the point $(X_{\rm NS}, 0, 0)$. To do so, we first introduce a function $f(y) = 1 - Ay$, where A is a constant defined by

$$A \equiv \Big(\frac{1}{H_{\rm ent}} \frac{\partial H_{\rm ent}}{\partial y} \Big) \Big|_{(X_{\rm NS},0,0)}. \qquad (47)$$

When we multiply this function by the enthalpy and define a modified enthalpy $H_{\rm mod} \equiv f H_{\rm ent}$, the modified enthalpy has its global maximum at the position $(X_{\rm NS}, 0, 0)$. During the iteration, this modified enthalpy term drags the neutron star to the proper position in the *Y*-direction. When the enthalpy maximum is properly located on the *X*-axis, we recover $A = 0$ and hence $f = 1$. We insert this procedure between (2f) and (2g) for the case of the Kerr-Schild background metric.

On the other hand, we have a $X-Z$ symmetry plane when using the isotropic background. Thus, the *Y*-derivative of the enthalpy always becomes zero on the *X*-axis, and the global maximum of the enthalpy must fall on the *X*-axis.

III. CODE TESTS

Our numerical code is based on the spectral methods libraries developed by the Meudon relativity group [35], and have been tested, used, and found to be highly accurate in several previous applications involving binary neutron stars [34, 36, 37, 38, 39, 40]. In the following we present some tests that verify our code for BHNS binaries. We present self-consistency tests, in which we explore the sensitivity of the results to changes in the position of the outer boundary, the type of boundary condition, and the number of collocation points used in the spectral method, and compare with analytical and previous numerical results.

A. Self-consistency tests

We present here the results of the self-consistency checks for a neutron star mass $\bar{M}_{\rm NS} = 0.05$. Our convergence criteria are chosen so that we iterate our solver until the relative difference in mass between the given value and our numerical result is less than one part in 10^{-7}. In the following tests, we will present values of the results with five digits, although this overstates their true accuracy, in order to show the magnitude of the changes in these quantities.

1. Position of the outer boundary

As long as the outer boundary of our computational domain is sufficiently far away from both the neutron star and the black hole, any physical quantities should be unaffected by the exact location of the outer boundary. Note that the outer boundary is located between the neutron star and the black hole in the present work (see Fig. 1). To test this, we set the orbital separation to $X_{\mathrm{NS}}/r_e = 10$, and change the position of the outer boundary from $R_{\mathrm{B}}/r_0 = 4$ to 9, where r_0 denotes the radius of a spherical neutron star with the same baryon rest-mass. In Table II, we show the orbital angular velocity ΩM_{BH}, the half-diameter of the neutron star $\bar{r}_e \equiv r_e/R_{\mathrm{poly}}$, and the maximum of the density quantity q_{max}. One can see from Table II that the radius of the neutron star and the maximum of the density quantity converge to better than order 10^{-5} for $5 < R_{\mathrm{B}}/r_0 \leq 8$, while the convergence of the orbital angular velocity is only of order 10^{-3} for a Kerr-Schild background and 10^{-4} for an isotropic background.

For a separation $X_{\mathrm{NS}}/r_e = 10$ and $\bar{M}_{\mathrm{NS}} = 0.05$, no position of the outer boundary larger than $R_{\mathrm{B}}/r_0 > 9.7$ is permitted because the boundary will overlap the black hole singularity. Even for a smaller value, the source terms of Eqs. (A1) – (A3) or (A12) – (A14) do not decrease sufficiently quickly with radius because of the contributions from the black hole background metric. Thus, we have to choose a position of the outer boundary for each orbital separation whose position is neither close to the neutron star nor to the black hole.

The relative error of the orbital angular velocity listed in Table II is larger for the Kerr-Schild background than for the isotropic background. This tendency results in part from the absence of the $X-Z$ plane symmetry in the Kerr-Schild background. We also see that the orbital angular velocity determined by using a larger outer boundary radius is slightly larger than that found using a smaller one. Because of this ambiguity, we will show only three significant digits in the final results.

2. Type of boundary condition

Next, we show in Table III the results of a comparison between our two different boundary conditions. The first is the multipole condition described in Sec. II E, and second is the condition in which only the leading-order, fall-off term is taken for each metric component. It is found that the relative difference in the orbital angular velocity is smaller than order 10^{-3} for the Kerr-Schild background and 10^{-4} for the isotropic background. The leading-order fall-off boundary condition seems to overestimate the angular velocity relative to the multipole condition. However, the relative error introduced by using different boundary conditions is an order of magnitude less than that introduced by changing the position of the outer boundary.

3. Number of collocation points

In the last self-consistency check we verify that physical quantities are largely independent of the number of collocation points $N_r \times N_\theta \times N_\varphi$ used in spectral field solver. Here, N_r, N_θ, and N_φ denote the number of collocation points in the radial, polar, and azimuthal directions, respectively. The orbital angular velocity seems to converge at a level of 10^{-4} in the Kerr-Schild background and $< 10^{-5}$ in the isotropic background, for any number of collocation points larger than $25 \times 17 \times 16$. Since the error in the orbital angular velocity is smaller than that induced by changing the position of the outer boundary for this number of points, we use a fixed number of collocation points $N_r \times N_\theta \times N_\varphi = 25 \times 17 \times 16$ to save computational time.

B. Comparison with previous results

To date, previous attempts to model equilibrium BHNS binary sequences have included the construction of a corotating relativistic star in a black hole background metric [31], a corotating Newtonian star in a black hole background metric computed in the tidal approximation [28], and a corotating or irrotational BHNS binary system in Newtonian gravity [29]. We now compare our relativistic results with these calculations.

1. Comparison with BSS

BSS provide results for a constant rest-mass sequence of corotating BHNS binaries in a Kerr-Schild background, with $\bar{M}_{\mathrm{NS}} = 0.05$ and $M_{\mathrm{BH}}/M_{\mathrm{NS}} = 10$. We compare our results at two of the orbital separations listed in their Table I, $d/r_e = 8$ and 5. Here d is the coordinate separation from the center of the black hole to the half-diameter of the neutron star on the X-axis, a quantity similar to their "$-x_{\mathrm{BH}}$". We define

$$d \equiv X_{\mathrm{NS}} + \frac{r_b - r_a}{2}, \qquad (48)$$

where r_a is the radius of the neutron star in the direction toward the black hole and r_b that to the opposite side (see Fig. 2). Since our definition of the orbital separation X_{NS} is different from that found in BSS, we have to transform our separation X_{NS} to d. However, since the relative difference between these two separations is less than 1% even for $d/r_e = 5$, our results are insensitive to the change up to three significant digits.

In Table V, we present the results of the comparison. Note that we show the results at $d/r_e = 5$ in the table here, but our results at this separation do not converge as well as our other results, only to the level of several parts in 10^{-5} in the relative error of the enthalpy between two successive iteration steps. Thus we do not include those

TABLE II: Convergence test for the position of the outer boundary R_B.

	Kerr-Schild: $\bar{M}_{NS} = 0.05$, $X_{NS}/r_e = 10.0$, $\bar{r}_0 = 1.1289$					
	Irrotation			Corotation		
R_B/r_0	ΩM_{BH}	$\bar{r}_e$	q_{max}	ΩM_{BH}	$\bar{r}_e$	q_{max}
4	9.7328(-3)	1.0964	0.023493	9.6399(-3)	1.1030	0.023339
5	9.7432(-3)	1.0962	0.023493	9.6500(-3)	1.1029	0.023338
6	9.7515(-3)	1.0962	0.023493	9.6580(-3)	1.1029	0.023338
7	9.7603(-3)	1.0962	0.023493	9.6664(-3)	1.1029	0.023338
8	9.7760(-3)	1.0962	0.023493	9.6807(-3)	1.1029	0.023337
9	9.9358(-3)	1.0964	0.023488	9.7890(-3)	1.1032	0.023330

	Isotropic: $\bar{M}_{NS} = 0.05$, $X_{NS}/r_e = 10.0$, $\bar{r}_0 = 1.1289$					
	Irrotation			Corotation		
R_B/r_0	ΩM_{BH}	$\bar{r}_e$	q_{max}	ΩM_{BH}	$\bar{r}_e$	q_{max}
4	9.1059(-3)	1.0960	0.023507	9.0364(-3)	1.1017	0.023376
5	9.1093(-3)	1.0960	0.023507	9.0397(-3)	1.1017	0.023376
6	9.1114(-3)	1.0960	0.023507	9.0418(-3)	1.1017	0.023376
7	9.1129(-3)	1.0960	0.023507	9.0432(-3)	1.1017	0.023376
8	9.1139(-3)	1.0960	0.023507	9.0443(-3)	1.1017	0.023376
9	9.1149(-3)	1.0960	0.023507	9.0452(-3)	1.1017	0.023376

TABLE III: Convergence test for the type of boundary condition.

			Kerr-Schild: $\bar{M}_{NS} = 0.05$					
			Irrotation			Corotation		
Boundary condition	X_{NS}/r_e	R_B/r_0	ΩM_{BH}	$\bar{r}_e$	q_{max}	ΩM_{BH}	$\bar{r}_e$	q_{max}
multipole	10.0	8	9.7760(-3)	1.0962	0.023493	9.6807(-3)	1.1029	0.023337
leading order	10.0	8	9.7799(-3)	1.0962	0.023493	9.6843(-3)	1.1029	0.023337
multipole	8.0	7	1.3588(-2)	1.1062	0.023429	1.3325(-2)	1.1186	0.023126
leading order	8.0	7	1.3627(-2)	1.1064	0.023427	1.3350(-2)	1.1188	0.023125
multipole	6.0	5	1.9457(-2)	1.1583	0.023193	1.8837(-2)	1.1818	0.022558
leading order	6.0	5	1.9478(-2)	1.1584	0.023192	1.8855(-2)	1.1817	0.022558

			Isotropic: $\bar{M}_{NS} = 0.05$					
			Irrotation			Corotation		
Boundary condition	X_{NS}/r_e	R_B/r_0	ΩM_{BH}	$\bar{r}_e$	q_{max}	ΩM_{BH}	$\bar{r}_e$	q_{max}
multipole	10.0	8	9.1139(-3)	1.0960	0.023507	9.0443(-3)	1.1017	0.023376
leading order	10.0	8	9.1152(-3)	1.0960	0.023507	9.0455(-3)	1.1017	0.023376
multipole	8.0	7	1.2430(-2)	1.1021	0.023467	1.2261(-2)	1.1126	0.023221
leading order	8.0	7	1.2432(-2)	1.1022	0.023467	1.2263(-2)	1.1126	0.023221
multipole	6.0	5	1.7811(-2)	1.1381	0.023315	1.7372(-2)	1.1580	0.022800
leading order	6.0	5	1.7816(-2)	1.1382	0.023315	1.7377(-2)	1.1581	0.022800

results in Sec. IV A, but show them here as a code test only.

Our results agree with those of BSS within 2%, even though we calculate them using a completely different numerical method.

2. *Comparison with the results by Ishii et al. [28]*

In [28], the critical value of a quantity

$$\mu \equiv \left(\frac{M_{NS}}{M_{BH}}\right)\left(\frac{X_{NS}}{r_0}\right)^3, \tag{49}$$

TABLE IV: Convergence test for the number of collocation points used in the spectral method field solver, $N_r \times N_\theta \times N_\varphi$.

	Kerr-Schild: $\bar{M}_{NS} = 0.05$, $X_{NS}/r_e = 10.0$, $R_B/r_0 = 8$					
	Irrotation			Corotation		
$N_r \times N_\theta \times N_\varphi$	ΩM_{BH}	$\bar{r}_e$	q_{max}	ΩM_{BH}	$\bar{r}_e$	q_{max}
$13 \times 9 \times 8$	9.8004(-3)	1.0961	0.023495	9.7019(-3)	1.1030	0.023338
$17 \times 13 \times 12$	9.7807(-3)	1.0962	0.023493	9.6849(-3)	1.1029	0.023337
$25 \times 17 \times 16$	9.7760(-3)	1.0962	0.023493	9.6807(-3)	1.1029	0.023337
$33 \times 21 \times 20$	9.7742(-3)	1.0962	0.023493	9.6792(-3)	1.1029	0.023337
$37 \times 25 \times 24$	9.7735(-3)	1.0962	0.023493	9.6785(-3)	1.1029	0.023337
	Isotropic: $\bar{M}_{NS} = 0.05$, $X_{NS}/r_e = 10.0$, $R_B/r_0 = 8$					
	Irrotation			Corotation		
$N_r \times N_\theta \times N_\varphi$	ΩM_{BH}	$\bar{r}_e$	q_{max}	ΩM_{BH}	$\bar{r}_e$	q_{max}
$13 \times 9 \times 8$	9.1144(-3)	1.0959	0.023511	9.0468(-3)	1.1016	0.023379
$17 \times 13 \times 12$	9.1140(-3)	1.0960	0.023507	9.0443(-3)	1.1017	0.023376
$25 \times 17 \times 16$	9.1139(-3)	1.0960	0.023507	9.0443(-3)	1.1017	0.023376
$33 \times 21 \times 20$	9.1139(-3)	1.0960	0.023507	9.0443(-3)	1.1017	0.023376
$37 \times 25 \times 24$	9.1139(-3)	1.0960	0.023507	9.0443(-3)	1.1017	0.023376

TABLE V: Comparison with the results of BSS, which are calculated in the Kerr-Schild background metric for corotating BHNS binaries. The neutron star has a baryon rest-mass $\bar{M}_{NS} = 0.05$, and the mass ratio is $M_{BH}/M_{NS} = 10$.

	d/r_e	d/M_{BH}	ΩM_{BH}	$\bar{r}_e$	q_{max}
BSS	8.0	17.8	0.0133	1.11	0.0235
Our results	8.0	17.9	0.0133	1.12	0.0231
BSS	5.0	12.6	0.0223	1.26	0.0223
Our results	5.0	12.7	0.0222	1.28	0.0219

was calculated for corotating BHNS binaries in Fermi normal coordinates. Here r_0 is the radius that a neutron star with the same mass would have in isolation. In these calculations, the neutron star is treated as a Newtonian star in the black hole background which is expanded up to fourth order in the parameter r_0/X_{NS}. The quantity above is defined such that if $\mu < \mu_{crit}$, the neutron star will be tidally disrupted by the black hole. By fitting their numerical results, they give an approximate formula for μ_{crit} which holds for separations $X_{NS} \geq 6M_{BH}$ with good accuracy. The formula, Eq. (186) of [28], is given by

$$\mu_{crit} \simeq 14.9 \left(1 + 0.80 \frac{r_0}{X_{NS}}\right) \tag{50}$$

for polytropic neutron star models with an adiabatic index $\Gamma = 2$.

We show the results of the comparison in Fig. 3. The thick solid and dashed lines correspond to sequences of corotating BHNS binaries with neutron star masses $\bar{M}_{NS} = 0.05$ and 0.1, respectively, while the filled circle

and square show the critical values for these sequences. These points are calculated by inserting the closest separation we obtained for the corotating state in the Kerr-Schild background case into Eq. (49). The thin dotted and dot-dashed lines denote the critical value given by Eq. (50) for neutron star masses $\bar{M}_{NS} = 0.05$ and 0.1, where we use the radius of a spherical neutron star with the same baryon rest-mass; $\bar{r}_0 = 1.1289$ for $\bar{M}_{NS} = 0.05$ and $\bar{r}_0 = 0.98972$ for $\bar{M}_{NS} = 0.1$. for drawing all critical points.

Evidently, our sequences do not quite reach the limits found in [28]. This may be because our spectral method is unable to treat the cusp-like features that appear at the inner Lagrange point when the neutron star fills out its Roche lobe. We can therefore approach the tidal break-up separation only up to a few percent, which may explain why our results for μ_{crit} are somewhat larger than those found in [28].

3. Comparison with the results by Uryu & Eriguchi [29]

In this section, we compare our results with those of [29], as was done by BSS with good agreement. In [29] sequences of BHNS binaries in Newtonian gravity were computed for both irrotational flow and corotation. For comparison, we select data with $N = 1.0$ and $M_S/M_{BH} = 0.1$ in their Table 2 for the corotating case, and in Table 4 for the irrotational case. Here, N denotes the polytropic index ($N \equiv 1/(\Gamma - 1)$) and M_S is the mass of the star (corresponding to M_{NS} here). We present the results of a comparison of the orbital angular velocity in Table VI. There, we compare our data for a neutron star mass $\bar{M}_{NS} = 0.05$ and mass ratio $M_{BH}/M_{NS} = 10$
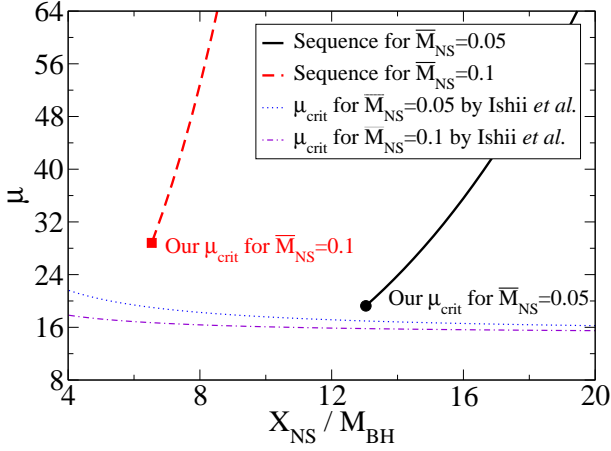
reasonable.

Comparison with Ishii *et al.*

FIG. 3: Critical value of the tidal disruption parameter μ as a function of the orbital separation. The thick solid and dashed lines represent sequences of corotating BHNS binaries with neutron star masses $\bar{M}_{\mathrm{NS}} = 0.05$ and 0.1, respectively; the filled circle and square show the critical values for both. The thin dotted and dot-dashed lines denote the critical values given by Eq. (50) for neutron star masses $\bar{M}_{\mathrm{NS}} = 0.05$ and 0.1.

TABLE VI: Comparison with the results of Uryu and Eriguchi [29]. The results are compared for a neutron star mass $\bar{M}_{\mathrm{NS}} = 0.05$ with mass ratio $M_{\mathrm{BH}}/M_{\mathrm{NS}} = 10$. Here, we use the radius of a spherical star, $\bar{r}_0 = 1.1289$, to convert their results into our units. K-S and ISO denote the respective backgrounds.

	Irrotation	Corotation
	ΩM_{BH}	ΩM_{BH}
Uryu & Eriguchi	0.0262	0.0264
Our results (K-S)	0.0224	0.0216
Our results (ISO)	0.0224	0.0217

in the Kerr-Schild and isotropic backgrounds. Since the sequences in [29] were computed using Newtonian gravity while we use full general relativity, we can compare only an invariant quantity, e.g., the orbital angular velocity. In order to convert their Newtonian results to values comparable to our relativistic ones, we scale our results by the radius of a relativistic spherical neutron star with mass $\bar{M}_{\mathrm{NS}} = 0.05$, $\bar{r}_0 = 1.1289$. Our results are shown at the closest separation we calculate, which is several percent further away in distance from the real tidal disruption point, because the spectral method is unable to treat cusp-like figures. Thus we find our calculated values are about 15 % smaller than those found in [29], but given that our configurations have separations several percent away from the real tidal disruption point, we can say that the agreement with the angular velocities in Table VI is

C. Comparison with the relativistic Keplerian velocity in the limit of extreme mass ratio

In the limit of an extreme mass ratio ($M_{\mathrm{BH}}/M_{\mathrm{NS}} \gg 1$), the neutron star orbits on a circular, test-particle geodesic. In this limit, we should recover Kepler's law, $\Omega = \sqrt{M_{\mathrm{BH}}/r^3}$, where r is the areal radius. In Kerr-Schild coordinates, the radial coordinate is areal, but in isotropic coordinates we have to transform according to

$$r = (\psi_{\mathrm{BH}}^{\mathrm{ISO}})^2 r_{\mathrm{ISO}} = \left(1 + \frac{M_{\mathrm{BH}}}{2r_{\mathrm{ISO}}}\right)^2 r_{\mathrm{ISO}}, \qquad (51)$$

where r_{ISO} denotes the isotropic radius. In Fig. 4, we present the results for a mass ratio $M_{\mathrm{BH}}/M_{\mathrm{NS}} = 100$ with neutron star masses of $\bar{M}_{\mathrm{NS}} = 0.05$, 0.1, and 0.15. It is obvious that our results are in good agreement with the Keplerian frequency for both irrotational and corotating flows.

IV. NUMERICAL RESULTS

All results presented in this Section are for a polytropic index $\Gamma = 2$. The computational grid is divided into four domains (see Fig. 1), each one of which is covered by $N_r \times N_\theta \times N_\varphi = 25 \times 17 \times 16$ collocation points. We focus on a mass ratio of $M_{\mathrm{BH}}/M_{\mathrm{NS}} = 10$ and present 12 different sequences including

- Kerr-Schild backgrounds and isotropic backgrounds

- irrotational and corotational fluid flow

- neutron star mass of $\bar{M}_{\mathrm{NS}} = 0.05$, 0.1, and 0.15.

The results are summarized in Tables VII – IX for Kerr-Schild backgrounds and X – XII for isotropic backgrounds. Note that an isolated neutron star with the adopted $\Gamma = 2$ polytropic EOS has a maximum mass $\bar{M}_{\mathrm{NS,max}} = 0.18$.

A. The Kerr-Schild background

In Figs. 5 – 7, we show contours of the neutron star baryon rest-mass density profile at the closest separation we calculate for neutron star masses $\bar{M}_{\mathrm{NS}} = 0.05$, 0.1, and 0.15, respectively. In each figure, the left panel shows the irrotational case and the right panel the corotating one. These figures correspond to the final lines in Tables VII – IX. Since the total shift vector induces an asymmetry in the neutron star with respect to the $X-Z$ plane for a Kerr-Schild background, one can see a visible tilt in the stellar figure.
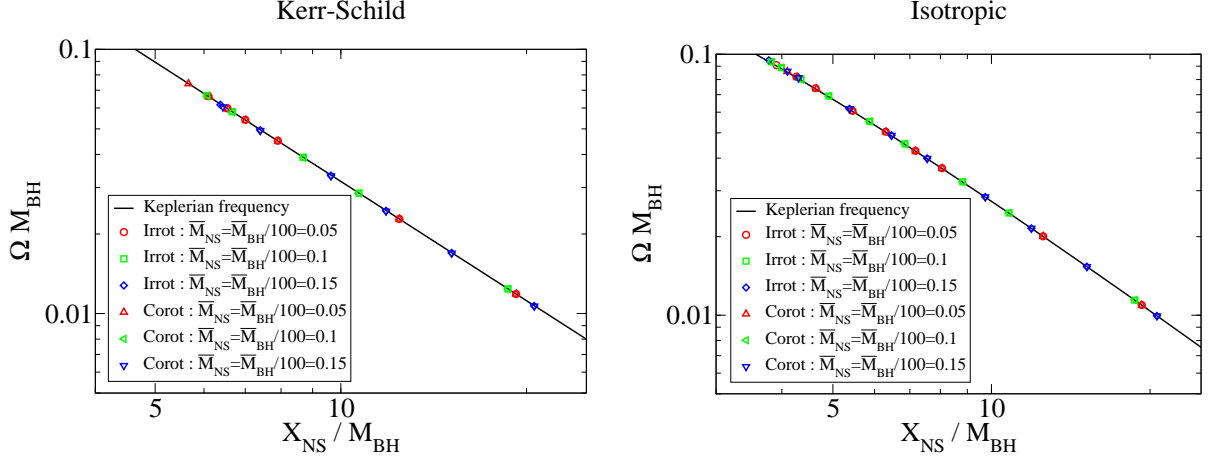
FIG. 4: The orbital angular velocity as a function of the orbital separation for a mass ratio $M_{BH}/M_{NS} = 100$. The left and right panels show Kerr-Schild and isotropic backgrounds, respectively. In each panel, we present six different sequences: two choices for the rotational state (irrotation and corotation) for each of three different neutron star masses ($\bar{M}_{NS} = 0.05$, 0.1, and 0.15). The solid line in each panel denotes the frequency of a Keplerian orbit. Note that the horizontal axis shows the X coordinate in Kerr-Schild coordinates in the left panel, but isotropic coordinates on the right.

TABLE VII: Physical parameters along a sequence with $M_{BH}/M_{NS} = 10$ in Kerr-Schild backgrounds. The orbital separation X_{NS}, orbital angular velocity Ω, half-diameter along the X-axis $\bar{r}_e$, maximum of the density parameter q_{max}, relative change in the central energy density δe, mass-shedding indicator χ, and radius of the outer boundary R_B are shown. The baryon rest-mass of the neutron star is $\bar{M}_{NS} = 0.05$. M_{NS}^G denotes the gravitational mass of a spherical neutron star with the same baryon rest-mass. M_{NS}^G/r_0 is the compaction parameter of an isolated neutron star.

Kerr-Schild: $\bar{M}_{NS} = 0.05$, $M_{NS}^G/r_0 = 0.0415$, $\bar{r}_0 = 1.1289$							
Irrotation							
X_{NS}/r_e	X_{NS}/M_{BH}	ΩM_{BH}	$\bar{r}_e$	q_{max}	δe	χ	R_B/r_0
10.0	21.9	9.78(-3)	1.10	0.0235	-2.41(-3)	0.977	8
8.0	17.7	1.36(-2)	1.11	0.0234	-5.16(-3)	0.908	7
7.0	15.7	1.62(-2)	1.12	0.0234	-8.39(-3)	0.834	6
6.0	13.9	1.95(-2)	1.16	0.0232	-1.54(-2)	0.699	5
5.2	12.8	2.24(-2)	1.23	0.0229	-2.89(-2)	0.505	5
Corotation							
X_{NS}/r_e	X_{NS}/M_{BH}	ΩM_{BH}	$\bar{r}_e$	q_{max}	δe	χ	R_B/r_0
10.0	22.1	9.68(-3)	1.10	0.0233	-9.17(-3)	0.957	8
8.0	17.9	1.33(-2)	1.12	0.0231	-1.83(-2)	0.875	7
7.0	15.9	1.58(-2)	1.14	0.0229	-2.73(-2)	0.793	6
6.0	14.2	1.88(-2)	1.18	0.0226	-4.30(-2)	0.654	5
5.2	13.0	2.16(-2)	1.25	0.0220	-6.51(-2)	0.460	5

In the left panel of Fig. 5, one can see a slight oscillation on the stellar surface. During the computation, we fit the boundary of the innermost domain to the stellar surface, allowing us to solve equilibrium configurations accurately, particularly in irrotational cases. Once a cusp develops on the stellar surface, it becomes impossible to adapt the innermost domain to the stellar surface. Using spectral methods, we express all quantities by summation over a finite number of differentiable functions. If we apply this method to such cusp-like figures, large numerical errors are induced. This situation is known as the Gibbs phenomenon. Since the stellar surface becomes highly distorted for very close configurations, even prior to the appearance of a cusp, we have to stop the sequence when such oscillations appear.

In order to investigate how close our results come to the

TABLE VIII: Same as Table VII, but for $\bar{M}_{NS} = 0.1$.

Kerr-Schild: $\bar{M}_{NS} = 0.1$, $M_{NS}^G/r_0 = 0.0879$, $\bar{r}_0 = 0.98972$							
Irrotation							
X_{NS}/r_e	X_{NS}/M_{BH}	ΩM_{BH}	$\bar{r}_e$	q_{max}	δe	χ	R_B/r_0
14.0	12.8	2.19(-2)	0.915	0.0585	-6.69(-3)	1.06	8
12.0	10.9	2.82(-2)	0.905	0.0582	-1.10(-2)	1.05	8
10.0	8.96	3.78(-2)	0.896	0.0577	-2.06(-2)	1.02	7
8.0	7.20	5.29(-2)	0.901	0.0564	-4.31(-2)	0.912	5.5
7.4	6.78	5.88(-2)	0.916	0.0554	-6.16(-2)	0.821	5.5
Corotation							
X_{NS}/r_e	X_{NS}/M_{BH}	ΩM_{BH}	$\bar{r}_e$	q_{max}	δe	χ	R_B/r_0
14.0	12.8	2.18(-2)	0.918	0.0582	-1.07(-2)	1.05	8
12.0	10.9	2.79(-2)	0.910	0.0578	-1.76(-2)	1.03	8
10.0	9.06	3.71(-2)	0.906	0.0570	-3.24(-2)	0.990	7
8.0	7.36	5.15(-2)	0.920	0.0550	-6.87(-2)	0.860	6
6.8	6.54	6.13(-2)	0.961	0.0527	-1.09(-1)	0.684	5

TABLE IX: Same as Table VII, but for $\bar{M}_{NS} = 0.15$.

Kerr-Schild: $\bar{M}_{NS} = 0.15$, $M_{NS}^G/r_0 = 0.145$, $\bar{r}_0 = 0.81526$							
Irrotation							
X_{NS}/r_e	X_{NS}/M_{BH}	ΩM_{BH}	$\bar{r}_e$	q_{max}	δe	χ	R_B/r_0
22.0	10.7	2.84(-2)	0.733	0.126	-5.76(-3)	1.10	8
20.0	9.65	3.34(-2)	0.724	0.126	-8.32(-3)	1.11	8
18.0	8.55	4.02(-2)	0.712	0.125	-1.26(-2)	1.13	8
16.0	7.45	4.97(-2)	0.698	0.124	-2.09(-2)	1.15	8
14.4	6.57	6.05(-2)	0.683	0.123	-3.04(-2)	1.16	8
Corotation							
X_{NS}/r_e	X_{NS}/M_{BH}	ΩM_{BH}	$\bar{r}_e$	q_{max}	δe	χ	R_B/r_0
22.0	10.8	2.83(-2)	0.734	0.126	-7.55(-3)	1.10	8
20.0	9.67	3.32(-2)	0.725	0.125	-1.09(-2)	1.11	8
18.0	8.58	3.99(-2)	0.715	0.125	-1.64(-2)	1.12	8
16.0	7.49	4.91(-2)	0.702	0.124	-2.68(-2)	1.13	8
14.0	6.41	6.27(-2)	0.686	0.121	-4.86(-2)	1.14	8

proper tidal disruption points, we introduce a sensitive numerical indicator for the mass-shedding point, defined as

$$\chi \equiv \frac{(\partial H_{ent}/\partial r)_{eq,comp}}{(\partial H_{ent}/\partial r)_{pole}}, \quad (52)$$

where the numerator denotes the radial derivative of enthalpy of the neutron star toward the companion star in the equatorial plane on the X-axis and the denominator that toward the pole of the neutron star. Both terms are evaluated on the stellar surface. This indicator takes the value unity at infinite orbital separation, and goes to zero at the mass-shedding point.

We show numerical results for χ in Fig. 8. The solid line with circles represents the irrotational case and the dashed line with squares the corotating one. As explained above, it is difficult for the spectral method to treat cusp-like figures, so we stop the calculation of sequences before reaching $\chi = 0$, which would correspond to the mass-shedding point. However, we can extrapolate our results in polynomial functions to predict the orbital separation at the tidal disruption point, $\chi = 0$. The extrapolations are shown as a dotted line for the irrotational case and a dot-dashed line for the corotating case in Figs. 8(a) and (b). For a neutron star of mass $\bar{M}_{NS} = 0.15$, we do not attempt to extrapolate our results to the tidal
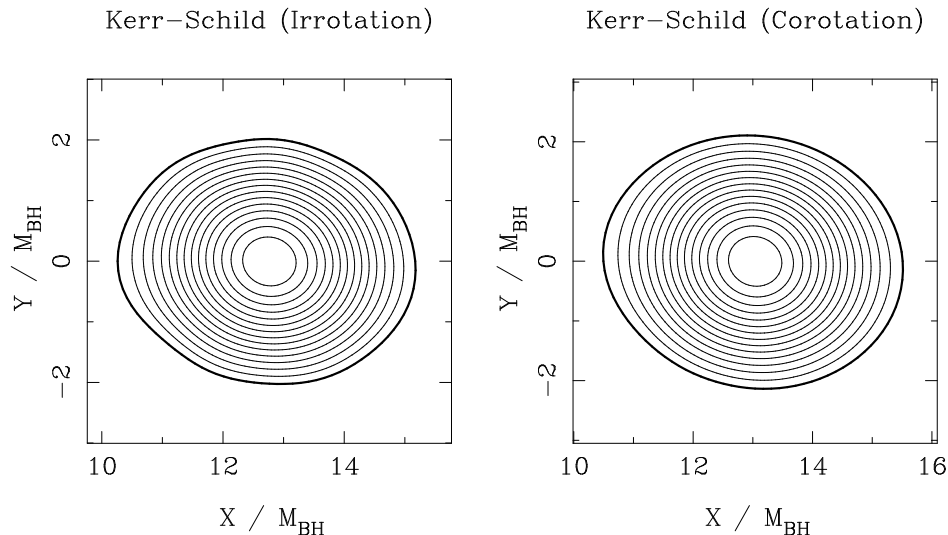
Kerr−Schild (Irrotation)   Kerr−Schild (Corotation)

FIG. 5: Baryon rest-mass density contours for a neutron star with $\bar{M}_{\mathrm{NS}} = 0.05$ in the Kerr-Schild background, at the point of closest binary separation along our sequence. The left and right panels show the irrotational and corotating cases, respectively. The position of the density maximum is $X_{\mathrm{NS}}/M_{\mathrm{BH}} = 12.8$ for the irrotational case and $X_{\mathrm{NS}}/M_{\mathrm{BH}} = 13.0$ for the corotating one.

Kerr−Schild (Irrotation)   Kerr−Schild (Corotation)
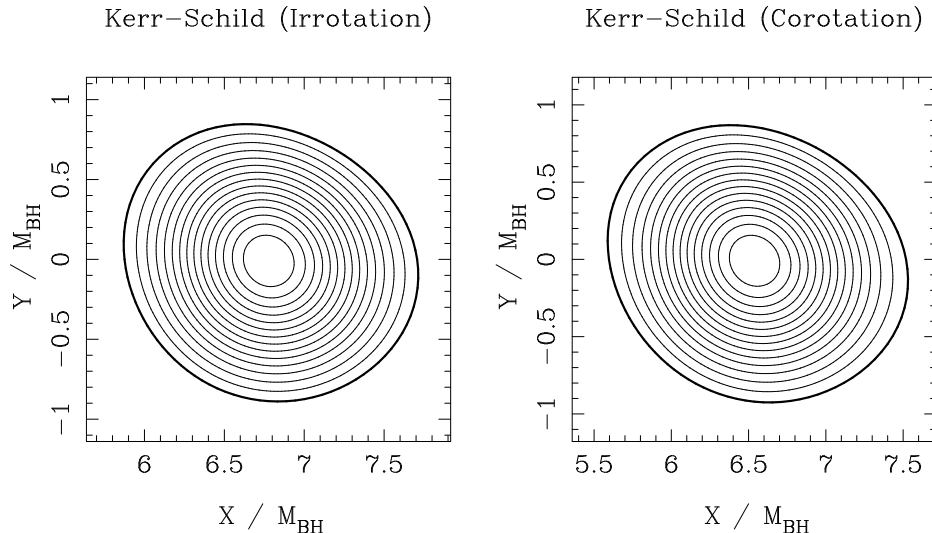
FIG. 6: Same as Fig. 5, but for $\bar{M}_{\mathrm{NS}} = 0.1$. The position of the density maximum is $X_{\mathrm{NS}}/M_{\mathrm{BH}} = 6.78$ for the irrotational case and $X_{\mathrm{NS}}/M_{\mathrm{BH}} = 6.54$ for the corotating one.

disruption limit because the closest separations we can calculate are too far away, for both rotation states, to make a reasonable fit. Clearly the extrapolation introduces considerable error, so that we are able to predict the tidal separation only with modest accuracy.

We find that the state of rotation has a small effect of a few percent on the tidal separation, which is in agreement with earlier findings (e.g. [27]). For $\bar{M}_{\mathrm{NS}} = 0.05$ we find approximately $r_{\mathrm{tid}} = 11.5 M_{\mathrm{BH}}$ (which is in good agreement with the value $11.9 M_{\mathrm{BH}}$ found in BSS), and for $\bar{M}_{\mathrm{NS}} = 0.1$ we find approximately $r_{\mathrm{tid}} = 5 M_{\mathrm{BH}}$.

Finally, we examine the relative change in the central energy density of the neutron star to that of an isolated, spherical neutron star with the same baryon rest-mass. Here, the total energy density and the relative change of its central value are, respectively, defined by $e \equiv \rho_0 + \rho_i$ and

$$\delta e \equiv \frac{e_c}{e_{c,0}} - 1, \qquad (53)$$

where e_c is the central energy density of the neutron star and $e_{c,0}$ that of a spherical neutron star with the same baryon rest-mass. We see from Tables VII – IX that
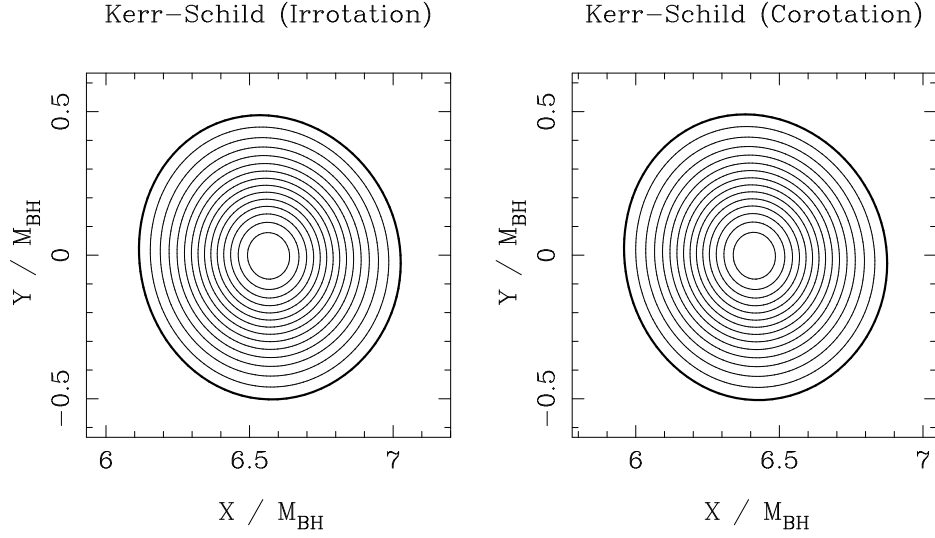
Kerr−Schild (Irrotation)   Kerr−Schild (Corotation)

FIG. 7: Same as Fig. 5, but for $\bar{M}_{\rm NS} = 0.15$. The position of the density maximum is $X_{\rm NS}/M_{\rm BH} = 6.57$ for the irrotational case and $X_{\rm NS}/M_{\rm BH} = 6.41$ for the corotating one.
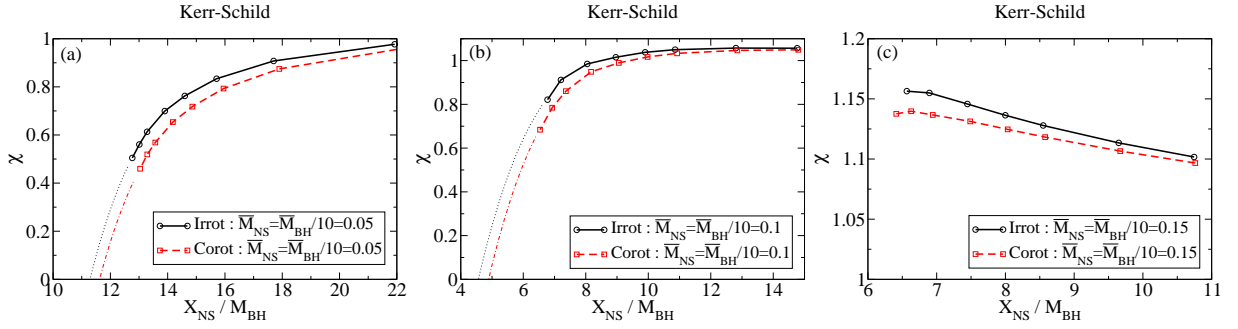

FIG. 8: Mass-shedding indicator χ, defined by Eq. (52), as a function of the orbital separation for the neutron star mass (a)$\bar{M}_{\rm NS} = 0.05$, (b)$\bar{M}_{\rm NS} = 0.1$ and (c)$\bar{M}_{\rm NS} = 0.15$, in Kerr-Schild backgrounds. Mass-shedding will begin when $\chi = 0$. The thick solid line with circles represents the irrotational case and the thick dashed line with squares the corotating one. The thin dotted and dot-dashed lines are extrapolations for the results of the irrotational and corotating cases, respectively.

the total energy density decreases as the orbital separation decreases for all sequences. At fixed orbital separation and neutron star mass, the decrease in the total energy density is larger for the corotating case than for the irrotational one. We attribute this effect to the neutron star spin, since the rotation expands the star's volume and results in a larger decrease in the central energy density. Roughly speaking, the amount of relative decrease of the central energy density at the mass-shedding point is $\sim 5\%$ for an irrotational neutron star of mass $\bar{M}_{\rm NS} = 0.05$, and $\sim 10\%$ for a corotating one, if we extrapolate our results. For a neutron star of mass $\bar{M}_{\rm NS} = 0.1$, the relative decrease is about $\sim 15\%$ for the irrotational case and about $\sim 20\%$ for the corotating one. This implies that a more massive neutron star undergoes a larger decrease in the energy density than a less massive one. We note that the central energy density

decreases monotonically, even when the half-diameter on the X-axis, $\bar{r}_e$, decreases, as we find for sequences with $\bar{M}_{\rm NS} = 0.1$ and 0.15. This occurs, in part, because $\bar{r}_e$ is measured as a coordinate length, not as the proper length. Also, the diameter along the X-axis is not the primary axis in Kerr-Schild coordinates, because the stellar configuration is tilted due to asymmetries.

B. The isotropic background

In Figs. 9 – 11, we show contours of the baryon rest-mass density for neutron stars in an isotropic background. As in the Kerr-Schild background, the left panel is for the irrotational case and the right panel for the corotating one. These figures are taken from the configurations shown on the last lines of Tables X – XII, the

TABLE X: Same as Table VII, but for isotropic backgrounds.

Isotropic: $\bar{M}_{\rm NS} = 0.05$, $M_{\rm NS}^G/r_0 = 0.0415$, $\bar{r}_0 = 1.1289$							
Irrotation							
$X_{\rm NS}/r_e$	$X_{\rm NS}/M_{\rm BH}$	$\Omega M_{\rm BH}$	$\bar{r}_e$	$q_{\max}$	δe	χ	$R_{\rm B}/r_0$
10.0	21.9	9.11(-3)	1.10	0.0235	-1.78(-3)	0.942	8
8.0	17.6	1.24(-2)	1.10	0.0235	-3.52(-3)	0.883	7
6.0	13.7	1.78(-2)	1.14	0.0233	-1.01(-2)	0.719	5
5.0	12.0	2.13(-2)	1.20	0.0231	-2.08(-2)	0.514	4.5
4.7	11.6	2.24(-2)	1.23	0.0230	-2.50(-2)	0.406	4
Corotation							
$X_{\rm NS}/r_e$	$X_{\rm NS}/M_{\rm BH}$	$\Omega M_{\rm BH}$	$\bar{r}_e$	$q_{\max}$	δe	χ	$R_{\rm B}/r_0$
10.0	22.0	9.04(-3)	1.10	0.0234	-7.49(-3)	0.925	8
8.0	17.8	1.23(-2)	1.11	0.0232	-1.42(-2)	0.855	7
6.0	13.9	1.74(-2)	1.16	0.0228	-3.25(-2)	0.681	5
5.0	12.2	2.07(-2)	1.22	0.0223	-5.35(-2)	0.495	4.5
4.7	11.8	2.17(-2)	1.26	0.0221	-6.21(-2)	0.413	4

TABLE XI: Same as Table X, but for $\bar{M}_{\rm NS} = 0.1$

Isotropic: $\bar{M}_{\rm NS} = 0.1$, $M_{\rm NS}^G/r_0 = 0.0879$, $\bar{r}_0 = 0.98972$							
Irrotation							
$X_{\rm NS}/r_e$	$X_{\rm NS}/M_{\rm BH}$	$\Omega M_{\rm BH}$	$\bar{r}_e$	$q_{\max}$	δe	χ	$R_{\rm B}/r_0$
14.0	12.9	1.94(-2)	0.919	0.0586	-3.62(-3)	0.980	8
10.0	9.01	3.15(-2)	0.901	0.0583	-8.74(-3)	0.936	7
8.0	7.16	4.27(-2)	0.895	0.0579	-1.66(-2)	0.863	6
6.0	5.51	5.96(-2)	0.919	0.0568	-3.70(-2)	0.659	4.5
5.6	5.24	6.35(-2)	0.936	0.0563	-4.55(-2)	0.577	4.5
Corotation							
$X_{\rm NS}/r_e$	$X_{\rm NS}/M_{\rm BH}$	$\Omega M_{\rm BH}$	$\bar{r}_e$	$q_{\max}$	δe	χ	$R_{\rm B}/r_0$
14.0	12.9	1.93(-2)	0.921	0.0585	-6.62(-3)	0.973	8
10.0	9.07	3.12(-2)	0.907	0.0579	-1.67(-2)	0.918	7
8.0	7.25	4.20(-2)	0.907	0.0571	-3.11(-2)	0.837	6
6.0	5.65	5.78(-2)	0.942	0.0550	-6.79(-2)	0.634	5
5.6	5.37	6.16(-2)	0.958	0.0545	-7.81(-2)	0.564	4.5

closest separation we compute for each sequence. One can clearly see that there exists a symmetry with respect to the X–Z plane in addition to the X–Y plane symmetry (equatorial plane symmetry) in isotropic background. The half-diameter of the neutron star along the X-axis, $\bar{r}_e$, should be elongated by the tidal force from the black hole, but as in the Kerr-Schild background it decreases as the orbital separation decreases for $\bar{M}_{\rm NS} = 0.1$ and 0.15, and then increases at closer separations for $\bar{M}_{\rm NS} = 0.1$ because of coordinate effects.

The indicator for mass-shedding from the neutron star, χ, is shown in Fig. 12. Solid lines with circles and dashed lines with squares in each panel represent the irrotational case and corotating one, respectively. The dotted lines are extrapolations of our data for the irrotational case and dot-dashed lines those for the corotating case shown in Figs. 12 (a) and (b). For isotropic backgrounds, χ does not exceed unity even for high compactness, and decreases monotonically when the orbital separation decreases. From the extrapolations, we see that the orbital separations at the mass-shedding point are $X_{\rm NS} \sim 10.5 M_{\rm BH}$ for $\bar{M}_{\rm NS} = 0.05$ and $X_{\rm NS} \sim 4 M_{\rm BH}$ for $\bar{M}_{\rm NS} = 0.1$ with an error of approximately 10%. These values are coordinate separations, and should therefore not be compared immediately with the results in a Kerr-Schild background. We will compare our findings in much

TABLE XII: Same as Table X, but for $\bar{M}_{\mathrm{NS}} = 0.15$

Isotropic: $\bar{M}_{\mathrm{NS}} = 0.15$, $M_{\mathrm{NS}}^{G}/r_0 = 0.145$, $\bar{r}_0 = 0.81526$							
Irrotation							
X_{NS}/r_e	$X_{\mathrm{NS}}/M_{\mathrm{BH}}$	ΩM_{BH}	$\bar{r}_e$	$q_{\max}$	δe	χ	R_{B}/r_0
20.0	9.75	2.83(-2)	0.732	0.126	-5.24(-3)	0.995	8
16.0	7.59	3.96(-2)	0.712	0.126	-9.67(-3)	0.988	8
12.0	5.46	6.06(-2)	0.682	0.124	-2.31(-2)	0.959	7
10.0	4.43	7.82(-2)	0.665	0.122	-4.22(-2)	0.913	6
9.0	3.96	8.94(-2)	0.659	0.120	-6.06(-2)	0.868	5.5
Corotation							
X_{NS}/r_e	$X_{\mathrm{NS}}/M_{\mathrm{BH}}$	ΩM_{BH}	$\bar{r}_e$	$q_{\max}$	δe	χ	R_{B}/r_0
20.0	9.77	2.82(-2)	0.733	0.126	-7.23(-3)	0.992	8
16.0	7.61	3.94(-2)	0.714	0.125	-1.35(-2)	0.982	8
12.0	5.50	6.00(-2)	0.687	0.123	-3.18(-2)	0.948	7
10.0	4.49	7.68(-2)	0.674	0.120	-5.60(-2)	0.899	6
9.4	4.20	8.30(-2)	0.671	0.119	-6.74(-2)	0.874	5.5
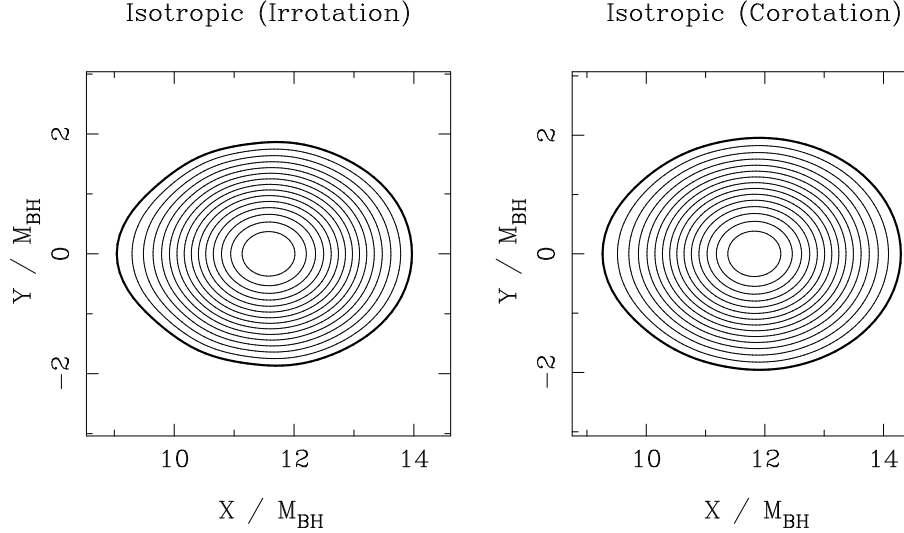
FIG. 9: Baryon rest-mass density contours for neutron stars with $\bar{M}_{\mathrm{NS}} = 0.05$ in an isotropic background, at the point of closest binary separation along our sequence. The left and right panels show the irrotational and corotating cases, respectively. The position of the density maximum is $X_{\mathrm{NS}}/M_{\mathrm{BH}} = 11.6$ for the irrotational case and $X_{\mathrm{NS}}/M_{\mathrm{BH}} = 11.8$ for the corotating one.

more detail in Section V. As before we do not extrapolate for $\bar{M}_{\mathrm{NS}} = 0.15$ because the closest separation we can calculate is still far from the mass-shedding point.

Since the indicator χ does not exceed unity for any sequence in an isotropic background and decreases monotonically toward zero, it is convenient to compare sequences for different neutron star masses $\bar{M}_{\mathrm{NS}}$ in the same figure. In Fig. 13, we show the mass-shedding indicator, χ, as a function of X_{NS}/r_e, for several different sequences. Interestingly, we see that χ is almost independent of the neutron star mass or spin, determined almost entirely by the normalized separation X_{NS}/r_e. A more massive neutron star has slightly smaller value of χ, indicating that it would be disrupted at a larger normalized separation X_{NS}/r_e. We can see the same behavior in the binary neutron stars, for example, in Fig. 7 of [38].

The central energy density again decreases for all sequences with the binary separation, as we found for all sequences in a Kerr-Schild background.
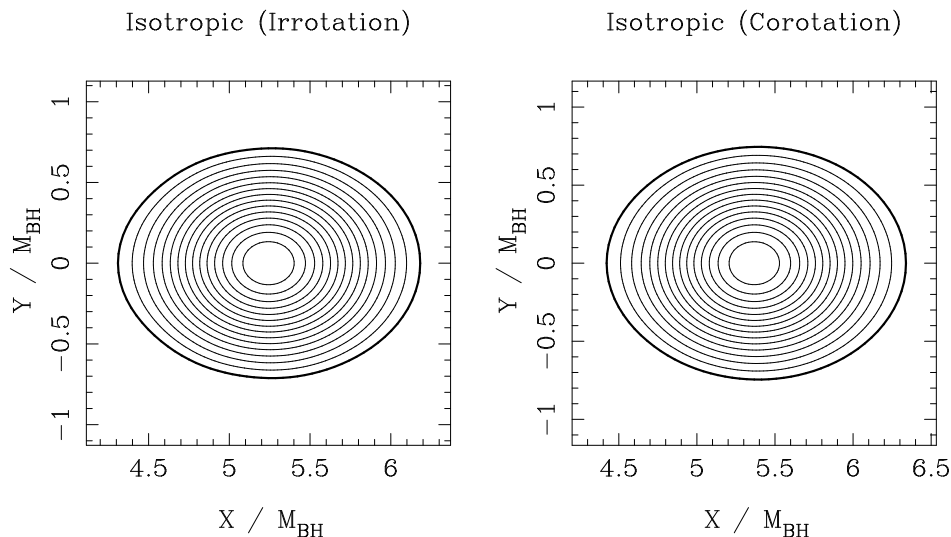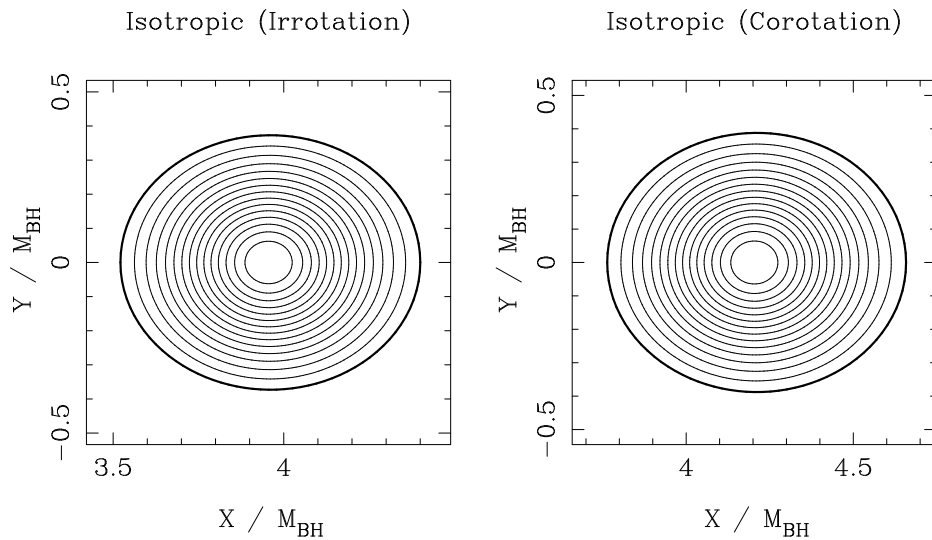
Isotropic (Irrotation)   Isotropic (Corotation)

FIG. 10: Same as Fig. 9, but for $\bar{M}_{\rm NS} = 0.1$. The position of the density maximum is $X_{\rm NS}/M_{\rm BH} = 5.24$ for the irrotational case and $X_{\rm NS}/M_{\rm BH} = 5.37$ for the corotating one.

Isotropic (Irrotation)   Isotropic (Corotation)

FIG. 11: Same as Fig. 9, but for $\bar{M}_{\rm NS} = 0.15$. The position of the density maximum is $X_{\rm NS}/M_{\rm BH} = 3.96$ for the irrotational case and $X_{\rm NS}/M_{\rm BH} = 4.20$ for the corotating one.

V. COMPARISON BETWEEN KERR-SCHILD AND ISOTROPIC BACKGROUNDS

Kerr-Schild coordinates and isotropic coordinates represent a Schwarzschild black hole in two different coordinate systems that differ not only in the spatial coordinates but also in the time-coordinate. Spatial slices in the two coordinate systems therefore represent distinct slices of Schwarzschild, and there is no reason to expect that solving the conformal thin-sandwich equations on these different slices will result in physically equivalent solutions.

It is of interest, then, to compare our results for Kerr-Schild and isotropic backgrounds. Most interesting, of course, are comparisons of coordinate-independent quantities, in particular the angular velocity (for example at tidal break-up), and the maximum density. We also include comparisons of the effective enthalpy and the shift vector, which behaves very differently in the two coordinate systems.
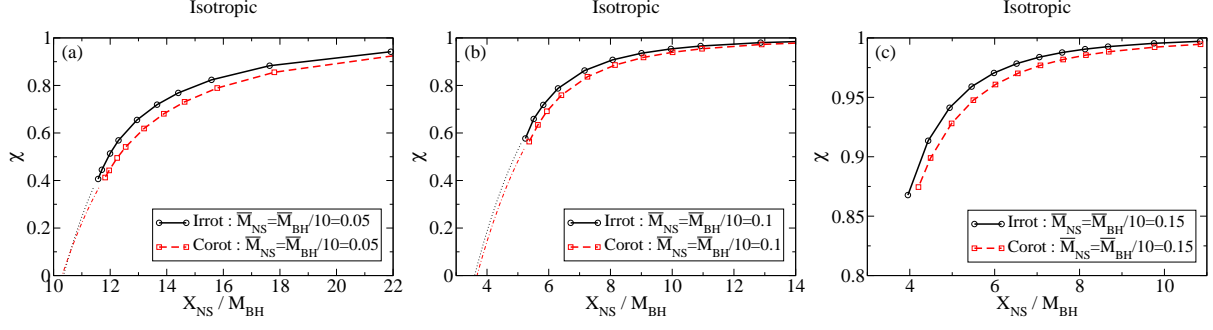
FIG. 12: Mass-shedding indicator χ, defined by Eq. (52), as a function of the orbital separation for neutron star of mass (a)$\bar{M}_{NS} = 0.05$, (b)$\bar{M}_{NS} = 0.1$ and (c)$\bar{M}_{NS} = 0.15$ in isotropic backgrounds. The thick solid line with circles represents the irrotational case and the thick dashed line with squares the corotating one. The thin dotted and dot-dashed lines are extrapolations of the results for the irrotational and corotating cases, respectively.
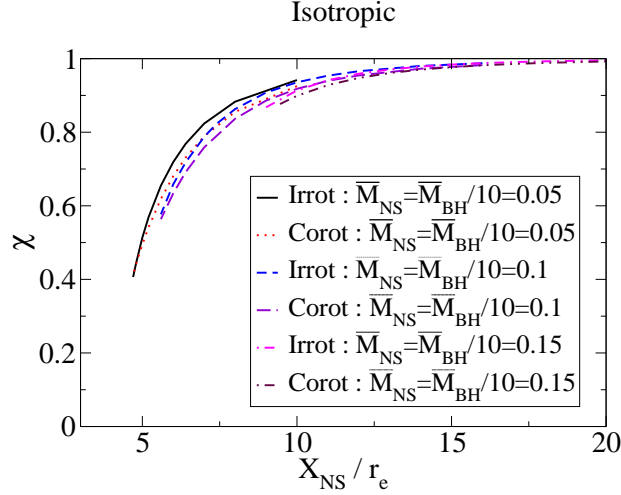
FIG. 13: Mass-shedding indicator χ as a function of the orbital separation X_{NS}/r_e. Solid, dashed, and dot-dashed lines denote the irrotational case with neutron star masses $\bar{M}_{NS} = 0.05$, 0.1, and 0.15, respectively. Dotted, long-dashed, and dot-dot-dashed lines are for the corotating case with $\bar{M}_{NS} = 0.05$, 0.1, and 0.15.

A. Orbital angular velocity at the mass-shedding point

As we explained previously, we stop the computation of each sequence before the mass-shedding point since it is impossible for the spectral method to treat cusp-like figures. Thus, we have to extrapolate all sequences to the mass-shedding point to estimate the value of the orbital angular velocity there. In Fig. 14, we show the mass-shedding indicator χ as a function of the orbital angular velocity. The indicator χ decreases rapidly as the separation decreases, or equivalently as the orbital angular velocity increases, so that extrapolating the curves using only our calculated values at large and medium separations may give predictions with large errors, especially for the irrotational case in the Kerr-Schild background

with $\bar{M}_{NS} = 0.05$; in cases where the sequences continue to smaller separations we expect an error of no more than $\sim 10\%$ in our measure of the terminal angular velocity.

For both Kerr-Schild and isotropic backgrounds, we find a value $\Omega M_{BH} \sim 0.025$ for the corotating case with neutron star mass $\bar{M}_{NS} = 0.05$, in good agreement with the results of BSS, who find $\Omega M_{BH} = 0.0241$ (see their Table 1).

Finally, we comment on the discrepancy in the extrapolation curve for the irrotational case in the Kerr-Schild background with $\bar{M}_{NS} = 0.05$. In this case, since we do not have results in the range $0 < \chi < 0.5$, we cannot draw an accurate extrapolation curve, as mentioned above, and thus cannot use it to predict the orbital angular velocity at the mass-shedding point with a high degree of certainty. However, we can predict that the real orbital

angular velocity at the mass-shedding point should be smaller than $\Omega M_{\mathrm{BH}} \sim 0.027$ the value given by Fig. 14, because the parameter χ decreases more rapidly at larger orbital angular velocities for the irrotational case as compared to the corotating one for the range $\chi < 0.5$ (see Section V.B of [36]). This means that the data points for the irrotational case of the Kerr-Schild background with $\bar{M}_{\mathrm{NS}} = 0.05$ are most likely to lie below the extrapolated line (solid line) in reality.

B. Maximum value of the density quantity

The density parameter q is a measure of the density as seen by a comoving observer, and is therefore gauge-invariant. In Fig. 15 we show its maximum value in the star as a function of the orbital angular velocity, which is also coordinate-independent. As we have discussed before, the maximum density decreases with binary separation in all cases, and decreases more rapidly for corotating configurations.

For $\bar{M}_{\mathrm{NS}} = 0.05$ we find only very small differences between Kerr-Schild and isotropic backgrounds (less than 1%). However, for $\bar{M}_{\mathrm{NS}} = 0.1$ the compaction parameter M_{NS}^G/r_0 (M_{NS}^G is the gravitational mass of an isolated neutron star and r_0 its radius) and hence relativistic effects are significantly larger, the differences increase noticeably. The difference between the two backgrounds is now in the order of 5%, meaning that the effect of the background is almost as large as that of the presence of a binary companion. We find in all cases the Kerr-Schild background leads to a greater decrease in the central density than an isotropic background.

C. Effective enthalpy field

For corotating configurations the definition of the enthalpy can be extended to regions outside the neutron star by virtue of Eq. (28). As discussed in BSS this "effective enthalpy field" plays the role of an effective potential, allows for the definition of a Roche lobe in a fully relativistic context, and is very useful for locating the onset of tidal disruption. To see this, we evaluate (28) for corotating binaries

$$H_{\mathrm{ent}} = C - \nu + \ln \gamma_0, \tag{54}$$

where C is a constant. Inserting the definition of ν (Eq. (8)) and γ_0 (Eq. (24)) for the corotating case, we obtain

$$H_{\mathrm{ent}} = C - \ln \alpha - \frac{1}{2} \ln \left(1 - \frac{\gamma_{ij}\beta^i\beta^j}{\alpha^2} \right). \tag{55}$$

In the Newtonian limit this reduces to

$$H_{\mathrm{ent}}^{\mathrm{Newt}} = C' - \phi + \frac{1}{2}(\Omega \times r)^2, \tag{56}$$

where ϕ denotes the total gravitational field and C' is an integration constant which is the Newtonian limit of C.

For irrotational configurations Eq. (28) depends on the solution of the continuity equation, which can only be solved in the stellar interior. In this case we cannot extend the definition of the enthalpy to regions outside the neutron star, meaning that a straight-forward definition of the effective potential is possible only for corotating configurations.

We show contours of the effective enthalpy field (55) in Figs. 16 and 17 for neutron star of mass $\bar{M}_{\mathrm{NS}} = 0.05$ and 0.1, respectively. In each figure, the left panel is for the Kerr-Schild background and the right panel for the isotropic one. In both figures, we show the position of the inner Lagrange point using the symbol "$\times$" and that of the outer one with "$+$". The equipotential surface passing through the inner Lagrange point defines the relativistic Roche lobe. It is clear that the neutron star in our results still fits well within its Roche lobe, but if we decrease the separation only a few percent further, we expect a rapid deformation on the inner edge as a cusp forms at the mass-shedding limit.

For the Kerr-Schild background the absence of a symmetry across the $X-Z$ plane is again quite noticeable, in that the Lagrange points do not lie on the X-axis. For an isotropic background, on the other hand, the presence of this symmetry force the Lagrange points to lie on the X-axis.

D. Shift vector

One of the most significant differences between the Kerr-Schild coordinate system and the isotropic one is the existence/absence of the black hole shift vector. In isotropic coordinates the background shift is zero, while for a Kerr-Schild background the main contribution to the total shift arises from the Schwarzschild background. We show the shift vector for an inertial observer, $\beta_{\mathrm{NS}}^i + \beta_{\mathrm{BH}}^i$, for corotating configurations with $\bar{M}_{\mathrm{NS}} = 0.05$ in Fig. 18. The left panel is for the Kerr-Schild case at the orbital separation $X_{\mathrm{NS}}/M_{\mathrm{BH}} = 13.0$ and the right panel for the isotropic case at $X_{\mathrm{NS}}/M_{\mathrm{BH}} = 11.8$. The neutron star rotates counterclockwise. It is evident that for the Kerr-Schild background the shift is dominated by the outward-pointing background contribution β_{BH}^i. The lack of a symmetry across the $X-Z$ plane is again quite obvious for the Kerr-Schild background.

VI. SUMMARY

We have computed quasiequilibrium sequences of BHNS binary systems in general relativity. Under the assumption of an extreme mass ratio, $M_{\mathrm{BH}} \gg M_{\mathrm{NS}}$, we have treated the contribution of the black hole gravitational field as a fixed background, adopting the Schwarzschild metric in both Kerr-Schild and isotropic coordinates. The neutron star is modeled as a relativistic polytropic EOS with adiabatic index $\Gamma = 2$. We have
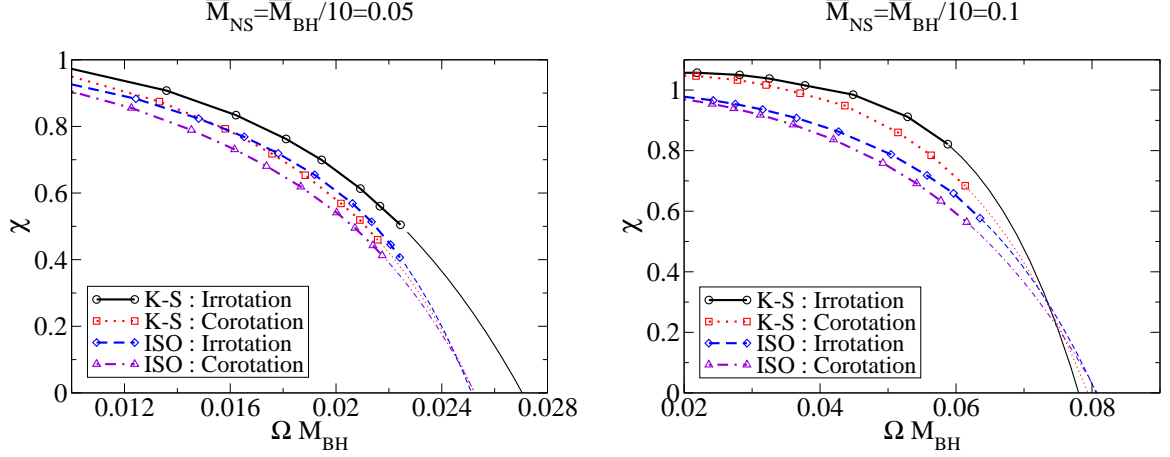
FIG. 14: The mass-shedding indicator χ as a function of the orbital angular velocity. The left panel shows sequences with neutron star mass $\bar{M}_{NS} = 0.05$, the right $\bar{M}_{NS} = 0.1$. K-S and ISO denote sequences performed in the respective backgrounds.
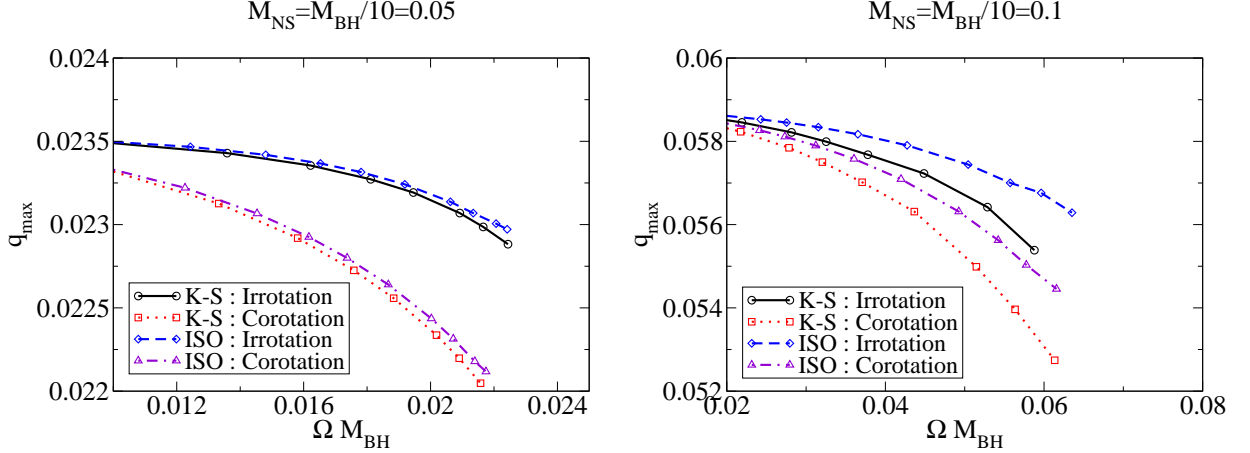

FIG. 15: Maximum value of the density quantity q_{max} as a function of the orbital angular velocity. The left panel corresponds to a neutron star of mass $\bar{M}_{NS} = 0.05$ the right panel $\bar{M}_{NS} = 0.1$. K-S and ISO denote the respective backgrounds.

solved a set of equations for two rotation states, irrotation and corotation. These results generalize those of BSS, which presented the first relativistic, self-consistent method to evaluate quasiequilibrium black hole-neutron star configurations.

We have developed a new numerical code for the present study, based on a spectral methods numerical approach that was used for a series of works on binary neutron stars [34, 36, 37, 38, 39, 40]. After confirming the validity of the numerical code in several tests, we have computed quasiequilibrium sequences of the BHNS binaries with a mass ratio $M_{BH}/M_{NS} = 10$ and neutron star masses $\bar{M}_{NS} = 0.05$, 0.1, and 0.15. We expect that spectral methods allow us to construct each individual model with greater accuracy than the finite difference methods

used by BSS. However, the assumption of smoothness inherent in spectral methods prevents us from constructing models very close to the onset of tidal disruption. This leads to errors in parameters describing the onset of tidal disruption that are greater than those obtained with finite differencing. While we maintain here some of the assumptions from BSS, including extreme mass ratios and polytropic equations of state, and plan to relax these in the near future.

In agreement with earlier studies (e.g. [27]), we find that the effect of rotation on the onset of tidal disruption is fairly small and in the order of a few percent. This does not rule out, however, that rotation has a larger effect on the dynamics of the tidal disruption itself (compare [14]). In particular, the rotational state of the neutron
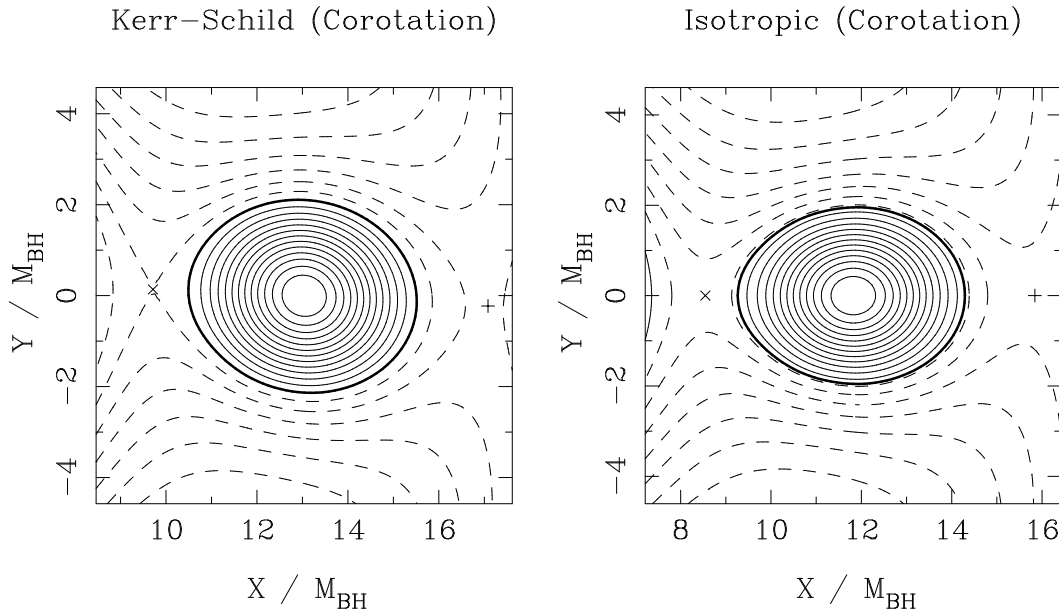
FIG. 16: Contours of the enthalpy field H_{ent} extended outside of the neutron star, which has a mass $\bar{M}_{\text{NS}} = 0.05$ and is corotating. The thick solid curve denotes the stellar surface, thin solid curves are contours located inside the neutron star, and dashed curves those outside. The left and right panels show configurations in the Kerr-Schild and isotropic backgrounds, respectively. Both depict the innermost point along the respective sequences, listed in the last line of the corresponding tables. The symbols $\times$ and $+$ denote the inner and outer Lagrange points, respectively. Note that the horizontal axis X in the left panel is the X coordinate of the Kerr-Schild coordinate system and that in the right panel is in the isotropic coordinate system.

star may well affect the size (or existence) of an accretion disk that may form as the neutron star is disrupted. Such an accretion disk is at the core of BHNS models as central engines of short-period gamma ray bursts (e.g. [8, 9, 10]).

We also find that the choice of background does have some effect on coordinate-independent quantities describing the resulting binary configurations. This indicates that the choice of background may affect the degree to which the solutions approximate quasiequilibrium, as well as the amount of spurious gravitational radiation inherent in the solutions. It will be very interesting to study these differences in future dynamical simulations (compare [14]).

APPENDIX A: EQUATIONS

In this appendix, we present the explicit forms of equations which we solve in our numerical code. Having applied the decompositions of metric quantities (18), (19), and (20) to the equations (7), (4), and (10), we can derive the final forms for the neutron star components in a numerically convenient form, inserting the black hole components as a fixed background.
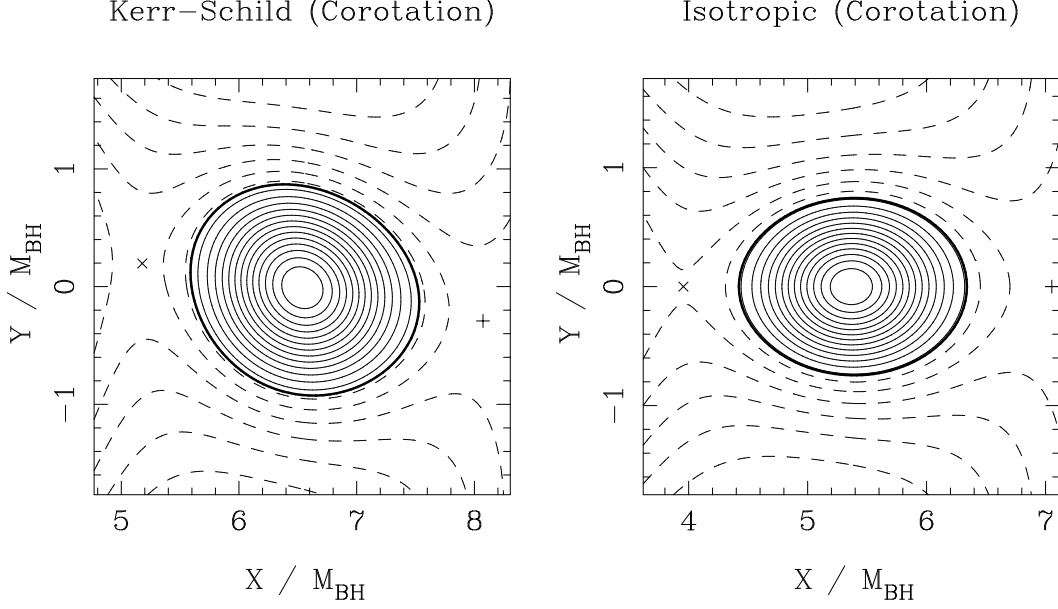
Kerr−Schild (Corotation)   Isotropic (Corotation)

FIG. 17: Same as Fig. 16, but for a neutron star of mass $\bar{M}_{\rm NS} = 0.1$.

1. Kerr-Schild background

a. Gravitational field equations

The equations (7), (4), and (10), respectively, can be written as

$$
\begin{aligned}
\underline{\Delta}\nu_{\rm NS} &= 4\pi\psi_{\rm NS}^4(\rho + S) + 2\alpha_{\rm BH}^2 H_{\rm BH} l^i l^j \bar{\nabla}_i \bar{\nabla}_j \nu_{\rm NS} \\
&+ \frac{\alpha_{\rm BH}^4 H_{\rm BH}}{r_{\rm BH}}\Big[2(1 + 4H_{\rm BH})l^i\bar{\nabla}_i\nu_{\rm NS} - l^i\bar{\nabla}_i\sigma_{\rm NS}\Big] \\
&+ \frac{\psi_{\rm NS}^{-8}}{\alpha_{\rm BH}^2}\tilde{A}_{ij}^{\rm NS}\tilde{A}_{\rm NS}^{ij} - \frac{4\psi_{\rm NS}^{-2}\alpha_{\rm BH}^2 H_{\rm BH}}{3\alpha_{\rm NS}r_{\rm BH}}(2 + 3H_{\rm BH})(3 + 4H_{\rm BH})l_i l_j \tilde{A}_{\rm NS}^{ij} \\
&- (\eta^{ij} - 2\alpha_{\rm BH}^2 H_{\rm BH} l^i l^j)(\bar{\nabla}_i\nu_{\rm NS})(\bar{\nabla}_j\sigma_{\rm NS}) - \frac{2\psi_{\rm NS}^4\alpha_{\rm BH}^4 H_{\rm BH}}{\alpha_{\rm NS}r_{\rm BH}^2}(2 + 10H_{\rm BH} + 9H_{\rm BH}^2)l_i\beta_{\rm NS}^i \\
&+ \frac{4\alpha_{\rm BH}^6 H_{\rm BH}^2}{3r_{\rm BH}^2}\Big[2\Big(\frac{\psi_{\rm NS}^4}{\alpha_{\rm NS}^2} - 1\Big)(2 + 3H_{\rm BH})^2 + (\psi_{\rm NS}^4 - 1)(1 + 3H_{\rm BH})^2 \\
&\qquad\qquad - 3\Big(\frac{\psi_{\rm NS}^4}{\alpha_{\rm NS}} - 1\Big)(2 + 10H_{\rm BH} + 9H_{\rm BH}^2)\Big],
\end{aligned} \tag{A1}
$$

$$
\begin{aligned}
\underline{\Delta}\sigma_{\rm NS} &= 4\pi\psi_{\rm NS}^4 S + 2\alpha_{\rm BH}^2 H_{\rm BH} l^i l^j \bar{\nabla}_i \bar{\nabla}_j \sigma_{\rm NS} + \frac{\alpha_{\rm BH}^4 H_{\rm BH}}{r_{\rm BH}}\Big[2(1 + 4H_{\rm BH})l^i\bar{\nabla}_i\sigma_{\rm NS} - l^i\bar{\nabla}_i\nu_{\rm NS}\Big] \\
&+ \frac{3\psi_{\rm NS}^{-8}}{4\alpha_{\rm BH}^2}\tilde{A}_{ij}^{\rm NS}\tilde{A}_{\rm NS}^{ij} - \frac{\psi_{\rm NS}^{-2}\alpha_{\rm BH}^2 H_{\rm BH}}{\alpha_{\rm NS}r_{\rm BH}}(2 + 3H_{\rm BH})(3 + 4H_{\rm BH})l_i l_j \tilde{A}_{\rm NS}^{ij} \\
&- \frac{1}{2}(\eta^{ij} - 2\alpha_{\rm BH}^2 H_{\rm BH} l^i l^j)\Big[(\bar{\nabla}_i\nu_{\rm NS})(\bar{\nabla}_j\nu_{\rm NS}) + (\bar{\nabla}_i\sigma_{\rm NS})(\bar{\nabla}_j\sigma_{\rm NS})\Big] \\
&- \frac{2\psi_{\rm NS}^4\alpha_{\rm BH}^4 H_{\rm BH}}{\alpha_{\rm NS}r_{\rm BH}^2}(2 + 10H_{\rm BH} + 9H_{\rm BH}^2)l_i\beta_{\rm NS}^i \\
&+ \frac{2\alpha_{\rm BH}^6 H_{\rm BH}^2}{r_{\rm BH}^2}\Big[\Big(\frac{\psi_{\rm NS}^4}{\alpha_{\rm NS}^2} - 1\Big)(2 + 3H_{\rm BH})^2 + (\psi_{\rm NS}^4 - 1)(1 + 3H_{\rm BH})^2
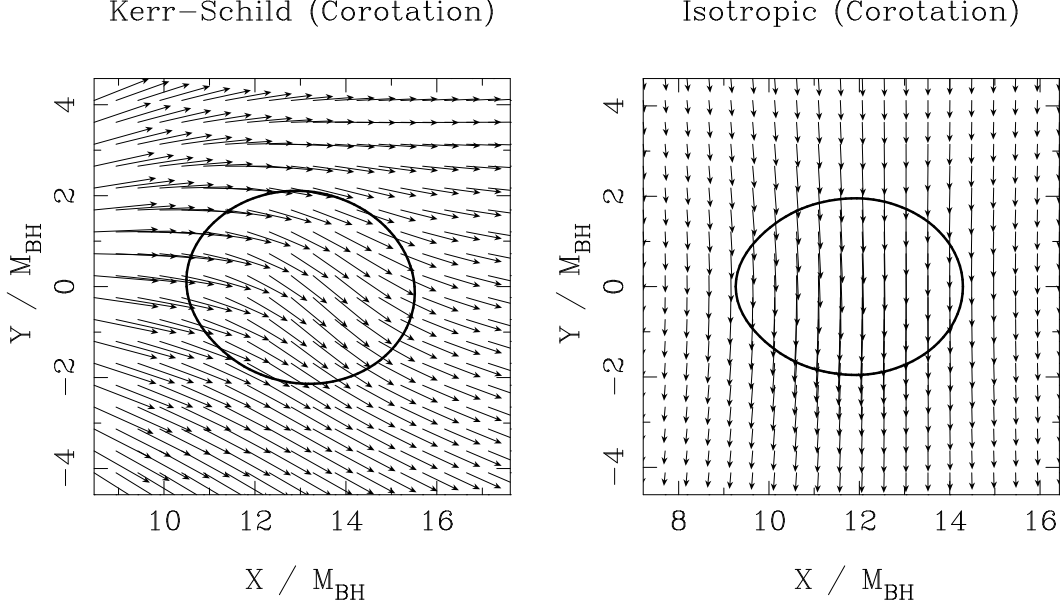\end{aligned}
$$

FIG. 18: Shift vectors seen by an inertial observer in the $X-Y$ plane (equatorial plane). The left and right panels show the Kerr-Schild and isotropic backgrounds, respectively. In both cases the neutron star has a mass $\bar{M}_{\mathrm{NS}} = 0.05$, and is corotating. Thick solid circles in each panel denote the stellar surface, and the arrows the direction of the shift vector. Note that the horizontal axis X in the left panel is the X coordinate of the Kerr-Schild coordinate system and that in the right panel is in the isotropic coordinate system.

$$-2\Big(\frac{\psi_{\mathrm{NS}}^4}{\alpha_{\mathrm{NS}}} - 1\Big)\big(2 + 10H_{\mathrm{BH}} + 9H_{\mathrm{BH}}^2\big)\Big], \tag{A2}$$

$$
\begin{aligned}
\underline{\Delta}\beta_{\mathrm{NS}}^i + \frac{1}{3}\bar{\nabla}^i\bar{\nabla}_j\beta_{\mathrm{NS}}^j &= 16\pi\alpha_{\mathrm{NS}}\alpha_{\mathrm{BH}}\psi_{\mathrm{NS}}^4 j^i + \frac{2}{3}\alpha_{\mathrm{BH}}^2 H_{\mathrm{BH}}\Big(3l^j l^k\bar{\nabla}_j\bar{\nabla}_k\beta_{\mathrm{NS}}^i + l^i l^k\bar{\nabla}_k\bar{\nabla}_j\beta_{\mathrm{NS}}^j\Big) \\
&\quad -\frac{\alpha_{\mathrm{BH}}^2 H_{\mathrm{BH}}}{r_{\mathrm{BH}}}\Big[4l^i\bar{\nabla}_j\beta_{\mathrm{NS}}^j - \alpha_{\mathrm{BH}}^2(3 + 8H_{\mathrm{BH}})l^j\bar{\nabla}_j\beta_{\mathrm{NS}}^i \\
&\qquad\qquad -\frac{1}{3}\Big\{\eta^{ij} + 2\alpha_{\mathrm{BH}}^2(9 + 11H_{\mathrm{BH}})l^i l^j\Big\}l_k\bar{\nabla}_j\beta_{\mathrm{NS}}^k\Big] \\
&\quad -\frac{2\alpha_{\mathrm{BH}}^4 H_{\mathrm{BH}}}{3r_{\mathrm{BH}}^2}\Big[(4 + 11H_{\mathrm{BH}})\beta_{\mathrm{NS}}^i - \alpha_{\mathrm{BH}}^2(12 + 51H_{\mathrm{BH}} + 46H_{\mathrm{BH}}^2)l^i l_j\beta_{\mathrm{NS}}^j\Big] \\
&\quad -\frac{8\alpha_{\mathrm{BH}}^8 H_{\mathrm{BH}}}{3r_{\mathrm{BH}}^2}(\alpha_{\mathrm{NS}} - 1)(2 + 10H_{\mathrm{BH}} + 9H_{\mathrm{BH}}^2)l^i - \frac{2\alpha_{\mathrm{NS}}}{\psi_{\mathrm{NS}}^6}\tilde{A}_{\mathrm{NS}}^{ij}\bar{\nabla}_j(3\sigma_{\mathrm{NS}} - 4\nu_{\mathrm{NS}}) \\
&\quad +\frac{2\alpha_{\mathrm{NS}}\alpha_{\mathrm{BH}}^2 H_{\mathrm{BH}}}{\psi_{\mathrm{NS}}^6 r_{\mathrm{BH}}}\tilde{A}_{\mathrm{NS}}^{ij}l_j \\
&\quad -\frac{4\alpha_{\mathrm{BH}}^6 H_{\mathrm{BH}}}{3r_{\mathrm{BH}}}(2 + 3H_{\mathrm{BH}})\Big[(1 + 2H_{\mathrm{BH}})\eta^{ij} - (3 + 2H_{\mathrm{BH}})l^i l^j\Big]\bar{\nabla}_j(3\sigma_{\mathrm{NS}} - 4\nu_{\mathrm{NS}}),
\end{aligned} \tag{A3}
$$

where $\underline{\Delta}$ and $\bar{\nabla}_i$ are the flat Laplace operator and partial derivative. The conformally related trace-free extrinsic curvature of the neutron star part is defined as

$$\tilde{A}_{\mathrm{NS}}^{ij} \equiv \frac{\psi_{\mathrm{NS}}^6}{2\alpha_{\mathrm{NS}}}\Big(\tilde{D}^i\beta_{\mathrm{NS}}^j + \tilde{D}^j\beta_{\mathrm{NS}}^i - \frac{2}{3}\tilde{\gamma}^{ij}\tilde{D}_k\beta_{\mathrm{NS}}^k\Big). \tag{A4}$$

b. Equation of continuity

Having defined a velocity field related to the orbital motion, i.e.,

$$W^i \equiv \psi^4 h \gamma_{\rm n} U_0^i, \tag{A5}$$

we can express the velocity potential as

$$\Psi = \Psi_0 + \eta_{ij} W_0^i x^j, \tag{A6}$$

where W_0^i is the constant value of W^i at the center of the neutron star, i.e.,

$$W_0^i \equiv (\psi^4 h \gamma_{\rm n} U_0^i)_{\rm center} = \text{constant}. \tag{A7}$$

Since the Newtonian limit of the right hand side of Eq. (A5) is the orbital motion $(\Omega \times r_{\rm BH})^i$, Eq. (A7) is merely the relativistic analogue of the translational motion of the center of the neutron star. Thus, the quantity Ψ_0 is regarded as the residual of the velocity potential, once the constant rotational component is subtracted away. The gradient of Ψ_0 yields the counter-rotation seen by a co-orbiting observer. The gradient and the Laplacian of Ψ_0 become

$$\bar{\nabla}^i \Psi = \bar{\nabla}^i \Psi_0 + W_0^i, \tag{A8}$$

$$\underline{\Delta} \Psi = \underline{\Delta} \Psi_0. \tag{A9}$$

Inserting the Kerr-Schild metric for the black hole into Eq. (32), we have our final form of the equation of continuity,

$$\zeta H_{\rm ent} \underline{\Delta} \Psi_0 + \Big[(1 - \zeta H_{\rm ent})(\bar{\nabla}^i H_{\rm ent} - 2\alpha_{\rm BH}^2 H_{\rm BH} l^i l^j \bar{\nabla}_j H_{\rm ent})$$

$$+ \zeta H_{\rm ent}(\bar{\nabla}^i \sigma_{\rm NS} - 2\alpha_{\rm BH}^2 H_{\rm BH} l^i l^j \bar{\nabla}_j \sigma_{\rm NS})$$

$$- 2\zeta H_{\rm ent} \frac{\alpha_{\rm BH}^4 H_{\rm BH}}{r_{\rm BH}}(1 + 4H_{\rm BH}) l^i \Big] \bar{\nabla}_i \Psi_0$$

$$= 2\zeta H_{\rm ent} \alpha_{\rm BH}^2 H_{\rm BH} l^i l^j \bar{\nabla}_i \bar{\nabla}_j \Psi_0 + (W^i - W_0^i) \bar{\nabla}_i H_{\rm ent} + \zeta H_{\rm ent} \frac{W^i}{\gamma_{\rm n}} \bar{\nabla}_i \gamma_{\rm n}$$

$$+ 2\zeta H_{\rm ent} \psi_{\rm NS}^4 h \gamma_{\rm n} \frac{\alpha_{\rm BH}^3 H_{\rm BH}}{r_{\rm BH}}(1 + 3H_{\rm BH})$$

$$+ \Big[\zeta H_{\rm ent} \bar{\nabla}_i (H_{\rm ent} - \sigma_{\rm NS}) - 2\alpha_{\rm BH}^2 H_{\rm BH} l_i \Big\{ \zeta H_{\rm ent} l^j \bar{\nabla}_j (H_{\rm ent} - \sigma_{\rm NS}) - l^j \bar{\nabla}_j H_{\rm ent} \Big\}$$

$$+ 2\zeta H_{\rm ent} \frac{\alpha_{\rm BH}^4 H_{\rm BH}}{r_{\rm BH}}(1 + 4H_{\rm BH}) l_i \Big] W_0^i. \tag{A10}$$

c. Determination of the orbital angular velocity

The left-hand side of the equation (42) can be expressed

$$\frac{\partial}{\partial X} \ln \gamma_0 \Big|_{(X_{\rm NS}, 0, 0)} = \frac{1}{2} \Big[1 - \frac{\psi^4}{\alpha^2} \Big\{ (\beta_{\rm I}^X)^2 (1 + 2H_{\rm BH}) + (\beta_{\rm I}^Y + \Omega X_{\rm NS})^2 + (\beta_{\rm I}^Z)^2 \Big\} \Big]^{-1}$$

$$\times \Big[\frac{\partial}{\partial X} \Big(\frac{\psi^4}{\alpha^2} \Big) \Big\{ (\beta_{\rm I}^X)^2 (1 + 2H_{\rm BH}) + (\beta_{\rm I}^Y + \Omega X_{\rm NS})^2 + (\beta_{\rm I}^Z)^2 \Big\}$$

$$+ 2 \Big(\frac{\psi^4}{\alpha^2} \Big) \Big\{ \beta_{\rm I}^X \frac{\partial \beta_{\rm I}^X}{\partial X} (1 + 2H_{\rm BH}) - (\beta_{\rm I}^X)^2 \frac{H_{\rm BH}}{r_{\rm BH}}$$

$$+ (\beta_{\rm I}^Y + \Omega X_{\rm NS}) \Big(\frac{\partial \beta_{\rm I}^Y}{\partial X} + \Omega \Big) + \beta_{\rm I}^Z \frac{\partial \beta_{\rm I}^Z}{\partial X} \Big\} \Big] \Big|_{(X_{\rm NS}, 0, 0)}, \tag{A11}$$

where $\beta_{\rm I}^i$ denotes the shift vector seen by the inertial observer, i.e., $\beta_{\rm I}^i \equiv \beta_{\rm NS}^i + \beta_{\rm BH}^i$.

The orbital angular velocity appears explicitly in the above equation, which corresponds to the left-hand side of Eq. (42). On the contrary, we compute the right-hand side of Eq. (42) in the form shown in which it is shown.

2. Isotropic background

a. Gravitational field equations

In the case of isotropic backgrounds, $\tilde{R}_{ij} = \tilde{R} = \tilde{A}_{\mathrm{BH}}^{ij} = K = 0$, because $\beta_{\mathrm{BH}}^{i} = 0$ and $\tilde{\gamma}_{ij} = \eta_{ij}$. This reduces the field equations to a much more simple form than those in Kerr-Schild backgrounds.

The equations (7), (4), and (10) are re-written as follows.

$$
\underline{\Delta}\nu_{\mathrm{NS}} = 4\pi\psi^4(\rho + S) + \psi^{-8}\tilde{A}_{ij}^{\mathrm{NS}}\tilde{A}_{\mathrm{NS}}^{ij} - (\bar{\nabla}_i\nu_{\mathrm{NS}})(\bar{\nabla}^i\sigma_{\mathrm{NS}})
$$
$$
- \frac{1}{\left(1 - \frac{M_{\mathrm{BH}}^2}{4r_{\mathrm{BH}}^2}\right)}\frac{M_{\mathrm{BH}}}{r_{\mathrm{BH}}^3}X^i\left[\frac{M_{\mathrm{BH}}}{2r_{\mathrm{BH}}}(\bar{\nabla}_i\nu_{\mathrm{NS}}) + (\bar{\nabla}_i\sigma_{\mathrm{NS}})\right], \tag{A12}
$$

$$
\underline{\Delta}\sigma_{\mathrm{NS}} = 4\pi\psi^4 S + \frac{3}{4}\psi^{-8}\tilde{A}_{ij}^{\mathrm{NS}}\tilde{A}_{\mathrm{NS}}^{ij} - \frac{1}{2}\left[(\bar{\nabla}_i\nu_{\mathrm{NS}})(\bar{\nabla}^i\nu_{\mathrm{NS}}) + (\bar{\nabla}_i\sigma_{\mathrm{NS}})(\bar{\nabla}^i\sigma_{\mathrm{NS}})\right]
$$
$$
- \frac{1}{\left(1 - \frac{M_{\mathrm{BH}}^2}{4r_{\mathrm{BH}}^2}\right)}\frac{M_{\mathrm{BH}}}{r_{\mathrm{BH}}^3}X^i\left[(\bar{\nabla}_i\nu_{\mathrm{NS}}) + \frac{M_{\mathrm{BH}}}{2r_{\mathrm{BH}}}(\bar{\nabla}_i\sigma_{\mathrm{NS}})\right], \tag{A13}
$$

$$
\underline{\Delta}\beta_{\mathrm{NS}}^i + \frac{1}{3}\bar{\nabla}^i\bar{\nabla}_j\beta_{\mathrm{NS}}^j = 16\pi\alpha\psi^4 j^i - \frac{2\alpha}{\psi^6}\tilde{A}_{\mathrm{NS}}^{ij}\bar{\nabla}_j\left[3(\sigma_{\mathrm{NS}} + \sigma_{\mathrm{BH}}) - 4(\nu_{\mathrm{NS}} + \nu_{\mathrm{BH}})\right]. \tag{A14}
$$

b. Equation of continuity

The equation of continuity (32) is written

$$
\zeta H_{\mathrm{ent}}\underline{\Delta}\Psi_0 + \left[(1 - \zeta H_{\mathrm{ent}})\bar{\nabla}^i H_{\mathrm{ent}} + \zeta H_{\mathrm{ent}}\left\{\bar{\nabla}^i\sigma_{\mathrm{NS}} + \frac{1}{\left(1 - \frac{M_{\mathrm{BH}}^2}{4r_{\mathrm{BH}}^2}\right)}\frac{M_{\mathrm{BH}}^2}{2r_{\mathrm{BH}}^4}X^i\right\}\right]\bar{\nabla}_i\Psi_0
$$
$$
= (W^i - W_0^i)\bar{\nabla}_i H_{\mathrm{ent}} + \zeta H_{\mathrm{ent}}\left[W_0^i\left\{\bar{\nabla}_i(H_{\mathrm{ent}} - \sigma_{\mathrm{NS}}) - \frac{1}{\left(1 - \frac{M_{\mathrm{BH}}^2}{4r_{\mathrm{BH}}^2}\right)}\frac{M_{\mathrm{BH}}^2}{2r_{\mathrm{BH}}^4}X_i\right\} + \frac{W^i}{\gamma_{\mathrm{n}}}\bar{\nabla}_i\gamma_{\mathrm{n}}\right].
$$
$$
\tag{A15}
$$

Here we have used the same quantities Φ_0, W^i, and W_0^i as defined in the Kerr-Schild part, Sec. A 1 b.

c. Determination of the orbital angular velocity

$$
\frac{\partial}{\partial X}\ln\gamma_0\Big|_{(X_{\mathrm{NS}},0,0)} = \frac{1}{2}\left[1 - \frac{\psi^4}{\alpha^2}\left\{(\beta_{\mathrm{NS}}^X)^2 + (\beta_{\mathrm{NS}}^Y + \Omega X_{\mathrm{NS}})^2 + (\beta_{\mathrm{NS}}^Z)^2\right\}\right]^{-1}
$$
$$
\times\left[\frac{\partial}{\partial X}\left(\frac{\psi^4}{\alpha^2}\right)\left\{(\beta_{\mathrm{NS}}^X)^2 + (\beta_{\mathrm{NS}}^Y + \Omega X_{\mathrm{NS}})^2 + (\beta_{\mathrm{NS}}^Z)^2\right\}\right.
$$
$$
+ \left(\frac{\psi^4}{\alpha^2}\right)\left\{\frac{\partial}{\partial X}\left((\beta_{\mathrm{NS}}^X)^2 + (\beta_{\mathrm{NS}}^Y)^2 + (\beta_{\mathrm{NS}}^Z)^2\right)\right.
$$
$$
\left.\left.+ 2\Omega\left(\beta_{\mathrm{NS}}^Y + X_{\mathrm{NS}}\frac{\partial\beta_{\mathrm{NS}}^Y}{\partial X}\right) + 2\Omega^2 X_{\mathrm{NS}}\right\}\right]\Big|_{(X_{\mathrm{NS}},0,0)}.
$$
$$
\tag{A16}
$$

Note here that since there is no black hole shift vector in the isotropic background, we write the shift vector seen by the inertial observer as β_{NS}^i.

[1] G. González and the LIGO Science Collaboration, Class. Quant. Grav. **21**, S691 (2004).

[2] M. Hewitson, P. Aufmuth, C. Aulbert, S. Babak, and R. Balasubramanian, Class. Quant. Grav **20**, 581 (2003).

[3] M. Ando and the TAMA collaboration, Class. Quant. Grav. **19**, 1409 (2002).

[4] F. Acernese and the VIRGO collaboration, Class. Quant. Grav. **21**, S709 (2004).

[5] K. Danzmann and the LISA study team, Class. Quant. Grav. **13**, A247 (1996).

[6] L. Blanchet, Living Rev. Rel. **5**, 3 (2002).

[7] T. W. Baumgarte and S. L. Shapiro, Phys. Rep. **376**, 41 (2003).

[8] H.-T. Janka, T. Eberl, M. Ruffert, and C.L. Fryer, Astrophys. J. Lett. **527**, L39 (1999)

[9] S. Rosswog, astro-ph/0505007.

[10] M. C. Miller, astro-ph/0505094.

[11] M. Vallisneri, Phys. Rev. Lett. **84**, 3519 (2000).

[12] B. Paczyński, Ann. Rev. Astron. Astrophys. **9**, 183 (1971).

[13] M. Shibata, Prog. Theor. Phys. **96**, 917 (1996).

[14] J. A. Faber, T. W. Baumgarte, S. L. Shapiro, K. Taniguchi, and F. A. Rasio, in preparation.

[15] B. Mashhoon, Astrophys. J. **197**, 705 (1975).

[16] B. Carter and J.-P. Luminet, Astron. Astrophys. **121**, 97 (1983); Mon. Not. R. Astron. Soc. **212**, 23 (1985).

[17] J.-A. Marck, Proc. R. Soc. London A **385**, 431 (1983).

[18] W. H. Lee and W. Kluzniak, Astrophys. J. **526**, 178 (1999); Mon. Not. R. Astron. Soc. **308**, 780 (1999).

[19] W. H. Lee, Mon. Not. R. Astron. Soc. **318**, 606 (2000); *ibid.* **328**, 583 (2001).

[20] S. Rosswog, R. Speith, and G. A. Wynn, Mon. Not. R. Astron. Soc. **351**, 1121 (2004).

[21] S. Kobayashi, P. Laguna, E. Sterl Phinney, and P. Mezaros, Astrophys. J. **615**, 855 (2004).

[22] D. Lai, F. A. Rasio, and S. L. Shapiro, Astrophys. J. Suppl. **88**, 205 (1993).

[23] S. Chandrasekhar, *Ellipsoidal Figures of Equilibrium* (Yale University Press, New Heaven, CT, 1969).

[24] L. G. Fishbone, Astrophys. J. **185**, 43 (1973).

[25] D. Lai and A. G. Wiseman, Phys. Rev. D **54**, 3958 (1996).

[26] K. Taniguchi and T. Nakamura, Prog. Theor. Phys. **96**, 693 (1996).

[27] P. Wiggins and D. Lai, Astrophys. J. **532**, 530 (2000).

[28] M. Ishii, M. Shibata, and Y. Mino, Phys. Rev. D **71**, 044017 (2005).

[29] K. Uryu and Y. Eriguchi, Mon. Not. R. Astron. Soc. **303**, 329 (1999).

[30] M. Miller, unpublished, gr-qc/0106017.

[31] T. W. Baumgarte, M. L. Skoge, and S. L. Shapiro, Phys. Rev. D **70**, 064040 (2004). [**BSS**]

[32] C. S. Kochanek, Astrophys. J. **398**, 234 (1992).

[33] L. Bildsten and C. Cutler, Astrophys. J. **400**, 175 (1992).

[34] E. Gourgoulhon, P. Grandclément, K. Taniguchi, J.-A. Marck, and S. Bonazzola, Phys. Rev. D **63**, 064029 (2001).

[35] http://www.lorene.obspm.fr/

[36] K. Taniguchi, E. Gourgoulhon, and S. Bonazzola, Phys. Rev. D **64**, 064012 (2001).

[37] K. Taniguchi and E. Gourgoulhon, Phys. Rev. D **65**, 044027 (2002).

[38] K. Taniguchi and E. Gourgoulhon, Phys. Rev. D **66**, 104019 (2002).

[39] K. Taniguchi and E. Gourgoulhon, Phys. Rev. D **68**, 124025 (2003).

[40] M. Bejger, D. Gondek-Rosinska, E. Gourgoulhon, P. Haensel, K. Taniguchi, and J. L. Zdunik, Astron. Astrophys. **431**, 297 (2005).

[41] S. Bonazzola, E. Gourgoulhon, and J.-A. Marck, Phys. Rev. D **58**, 104020 (1998).

[42] P. Grandclément, S. Bonazzola, E. Gourgoulhon, and J.-A. Marck, J. Comput. Phys. **170**, 231 (2001).

[43] We point out that we treat the Kerr-Schild and isotropic backgrounds slightly differently. For a Kerr-Schild background, the conformally related background metric $\tilde{\gamma}_{ij}$ is identified with the spatial metric γ_{ij} of a Kerr-Schild metric. For Schwarzschild in isotropic coordinates, the spatial metric is $\gamma_{ij} = \psi_{\mathrm{BH}}^4 \eta_{ij}$. In this case we absorb ψ_{BH} in our conformal factor ψ (see equation (17)), and identify the conformally related metric $\tilde{\gamma}_{ij}$ with the flat metric η_{ij}.

[44] H.-J. Yo, J. N. Cook, S. L. Shapiro, and T. W. Baumgarte, Phys. Rev. D **70** 084033 (2004); *ibid.* **70** 089904(E) (2004).

[45] S. Bonazzola, E. Gourgoulhon, and J.-A. Marck, Phys. Rev. D **56**, 7740 (1997).

[46] H. Asada, Phys. Rev. D **57**, 7292 (1998).

[47] M. Shibata, Phys. Rev. D **58**, 024012 (1998).

[48] S. A. Teukolsky, Astrophys. J. **504**, 442 (1998).

[49] See [50] for the transformation among these formulations [45, 46, 47, 48].

[50] E. Gourgoulhon, unpublished, gr-qc/9804054.